Title

The response of the $^{18}O/^{16}O$ composition of atmospheric CO_2 to changes in environmental conditions

Journal

Journal of Geophysical Research: Biogeosciences, 119(1)

ISSN

21698953

Authors

Buenning, Nikolaus
Noone, David
Randerson, James
et al.

Publication Date

2014

DOI

10.1002/2013JG002312

JOURNAL OF GEOPHYSICAL RESEARCH: BIOGEOSCIENCES, VOL. 119, 55–79, doi:10.1002/2013JG002312, 2014

The response of the $^{18}O/^{16}O$ composition of atmospheric CO_2 to changes in environmental conditions

Nikolaus Buenning,[1,2,3] David Noone,[1,2] James Randerson,[4] William J. Riley,[5] and Christopher Still[6]

Received 12 February 2013; revised 16 November 2013; accepted 23 November 2013; published 15 January 2014.

[1] This study investigates the response of the global mean and spatial variations of the $\delta^{18}O$ value of atmospheric CO_2 (δC_a) to changes in soil CO_2 hydration rates, relative humidity, the $\delta^{18}O$ value of precipitation and water vapor, visible radiation, temperature, and ecosystem flux partitioning. A three-dimensional global transport model was coupled to a mechanistic land surface model and was used to calculate isotopic fluxes of CO_2 and H_2O and the resulting δC_a. The model reproduced the observed global mean and north-south gradient in δC_a. The simulated seasonal amplitude and phases of CO_2 and δC_a agreed well at some but not all locations. Sensitivity tests with relative humidity increased by 3.2% from its original value decreased δC_a by 0.21‰. Similarly, a global 3.3‰ decrease in the isotopic composition of both precipitation and water vapor (δW_P and δW_{AV}, respectively) caused a 2.6‰ decrease in δC_a. A 1 K increase in atmospheric temperatures also affected δC_a, but there was a very small δC_a response to realistic changes in light levels. Experiments where leaf and soil CO_2 fluxes were repartitioned revealed a nontrivial change to δC_a. The predicted north-south δC_a gradient increased in response to an increase in soil CO_2 hydration rates. However, the δC_a gradient also had a large response to global changes in δW_P and δW_{AV}. This result is particularly important since most models fail to deplete δW_P enough at middle and high latitudes, where the influence of δW_P and δW_{AV} on the δC_a gradient is strongest.

Citation: Buenning, N., D. Noone, J. Randerson, W. J. Riley, and C. Still (2014), The response of the $^{18}O/^{16}O$ composition of atmospheric CO_2 to changes in environmental conditions, *J. Geophys. Res. Biogeosci.*, *119*, 55–79, doi:10.1002/2013JG002312.

1. Introduction

[2] Land use changes and rising levels of industrial activity have increased the atmospheric CO_2 concentration over the past several decades [*Denman et al.*, 2007; *Ballantyne et al.*, 2012]. Nevertheless, terrestrial photosynthesis and respiration still play a dominant role in the seasonal cycling of CO_2, annually exchanging 21% of the atmospheric stock [*Sarmiento and Gruber*, 2002]. A number of approaches have been developed to attribute observed atmospheric CO_2 concentration variations to its various surface sources and sinks, including inversions [*Gurney et al.*, 2003, 2004], bottom-up approaches [*Denman et al.*, 2007], and isotopic tracers (^{13}C, ^{14}C, and ^{18}O) [*Quay et al.*, 1992; *Fung et al.*, 1997; *Peylin et al.*, 1999; *Ogée et al.*, 2004; *Naegler et al.*, 2006; *Rayner et al.*, 2008]. This study focuses on the sensitivity of the $^{18}O/^{16}O$ composition of atmospheric CO_2 (hereafter δC_a, where $\delta = R/R_{\text{Standard}} - 1$ and R is the molar ratio of heavy to light isotopes, in the case of $^{18}O/^{16}O$) to changes in climate forcing. Since δC_a variations are believed to be driven primarily by terrestrial respiratory and photosynthetic fluxes, combined with the ^{18}O content of water in soils and plant leaves [*Francey and Tans*, 1987; *Farquhar et al.*, 1993; *Ciais et al.*, 1997a; *Cuntz et al.*, 2003a], δC_a is a potentially valuable atmospheric tracer of global interactions between the water and carbon cycles and of the separate contributions of each gross terrestrial carbon flux.

[3] *Francey and Tans* [1987] used global atmospheric observations to argue that terrestrial carbon fluxes were the most important influence on the north-south gradient in δC_a. *Farquhar et al.* [1993] confirmed this inference through a pioneering global model analysis, which showed that terrestrial ecosystem fluxes largely determine the spatial structure of δC_a. Studies using more complex global-scale models have concluded that both the north-south gradient and the seasonal cycle in δC_a are almost entirely determined by land ecosystem fluxes and atmospheric transport [*Ciais et al.*, 1997a, 1997b; *Peylin et al.*, 1999; *Cuntz et al.*, 2003a, 2003b; *Wingate et al.*, 2009]. The strong influence

---

[1] Department of Atmospheric and Oceanic Sciences, University of Colorado Boulder, Boulder, Colorado, USA.

[2] Cooperative Institute of Research in Environmental Sciences, University of Colorado Boulder, Boulder, Colorado, USA.

[3] Now at Department of Earth Sciences, University of Southern California, Los Angeles, California, USA.

[4] Department of Earth System Science, University of California, Irvine, California, USA.

[5] Earth Sciences Division Lawrence, Berkeley National Laboratory, Berkeley, California, USA.

[6] Forest Ecosystems and Society, Oregon State University, Corvallis, Oregon, USA.

Corresponding author: N. Buenning, University of Southern California, Department of Earth Sciences, 3651 Trousdale Pkwy., Los Angeles, CA 90089–0740, USA. (buenning@usc.edu)

2169-8953/14/10.1002/2013JG002312

of ecosystem fluxes is in part due to the equator-to-pole gradient in the $^{18}O/^{16}O$ composition of precipitation and water vapor. Furthermore, *Still et al.* [2009] demonstrated through site-level observations and an isotope-enabled land model a range of linkages between δC_a and the atmospheric hydrological cycle (such as humidity and cloud cover variations). Similarly, *Buenning et al.* [2011] and *Welp et al.* [2011] showed observational evidence of a possible connection between δC_a and both relative humidity and precipitation $\delta^{18}O$ values on interannual time scales. *Buenning et al.* [2011] also concluded that global mechanistic models would be needed to test their proposed hypotheses. *Wingate et al.* [2009] presented global model experiments that showed how an increased soil CO_2 hydration rate reduced discrepancies between observed and modeled δC_a. In particular, their results suggested that high CO_2 hydration rates in soils are necessary to correctly simulate the north-south gradient in δC_a. However, their study did not evaluate how other variables could also change the simulated gradient to better match observations. In fact, there remains a need to obtain and provide extensive, model-based quantitative estimates of the response of δC_a and the north-south δC_a gradient to changes in environmental conditions. In this study, we used a global-scale model of CO_2 and $CO^{18}O$ exchanges to examine the sensitivity of the annual mean and spatial variations of δC_a to changes in climatic variables that could potentially influence δC_a.

[4] In Appendix B, the δC_a budget is examined and the potential driving variables are identified as relative humidity, $\delta^{18}O$ values of precipitation and vapor, radiation levels, temperature, and ecosystem flux partitioning. To evaluate the climatic and ecosystem influences on δC_a, land simulations were performed using an isotope-enabled version of the National Center for Atmospheric Research (NCAR) Land Surface Model (ISOLSM) [*Bonan*, 1996; *Riley et al.*, 2002, 2003; *Lai et al.*, 2006], similar to that used by *Still et al.* [2009]. The simulations used predicted global surface-to-atmosphere fluxes from ISOLSM as input to the NCAR Community Atmosphere Model (CAM) to estimate δC_a. This model configuration allows us to easily conduct the sensitivity experiments described below. A comparison between a control simulation and observed δC_a is presented to demonstrate model performance. We conducted sensitivity experiments with the model to determine how changes in soil CO_2 hydration, relative humidity, the $\delta^{18}O$ value of precipitation and water vapor, light levels, temperature, and ecosystem CO_2 fluxes can affect the annual mean and spatial δC_a variations via changes in gross CO_2 fluxes and/or the isotopic composition of leaf and soil water.

2. Model and Experiments

2.1. The Land Surface Model (ISOLSM)

[5] Land Surface Model simulates the exchanges of energy, momentum, H_2O, and CO_2 between the atmosphere and the terrestrial biosphere. *Riley et al.* [2002, 2003] developed integrated modules within LSM1.0 (together called ISOLSM) to compute the exchanges of $CO^{18}O$ and $H_2{}^{18}O$ to and from the terrestrial biosphere. The model calculates canopy water vapor, vertically resolved soil water, and shaded and sunlit leaf water, as well as the ^{18}O (and ^2H) isotopic composition of each pool. Nine model layers are used for the simulations, with increasing thickness with depth (dz = 0.04, 0.04, 0.04, 0.1, 0.2, 0.4, 0.8, 1.6, and 3.2 m).

[6] ISOLSM accounts for ^{18}O in water and CO_2 exchanges by including various kinetic and equilibrium fractionation processes [*Riley et al.*, 2002]. A steady state estimate of canopy vapor and its isotopic composition is calculated via a mass balance equation dependent on fluxes and the isotopic content of atmospheric vapor, canopy transpiration and evaporation, and soil evaporation [*Riley et al.*, 2002, equation (11)]. A canopy turnover time (3 h) is then applied to the steady state value and the values from the previous time step. The leaf water model in ISOLSM employs a time-dependent mass balance that includes a transpiration-dependent leaf turnover time scale to calculate δW_l [*Dongmann et al.*, 1974; *Still et al.*, 2009]. The model uses an advective transport model for soil water, nonfractionating root water uptake, and surface boundary layer resistance to predict the soil water isotopic ratio. The $\delta^{18}O$ value of CO_2 within leaves and the soil column is predicted considering gaseous diffusion, surface boundary layer resistance, and the following temperature-dependent equilibration between gaseous CO_2 and water [*Brenninkmeijer et al.*, 1983]:

$$\alpha_{\mathrm{eq}}(T_s) = 1 + \left(\frac{17604}{T_s} - 17.93\right) \times 10^{-3} \tag{1}$$

where T_s (K) is surface temperature (i.e., ground or leaf temperature). Kinetic isotopic fractionation associated with CO_2 diffusion across the leaf stomata and modified for the leaf boundary layer is weighted by CO_2 concentration gradients from the canopy to the chloroplasts (following *Farquhar and Lloyd* [1993]). A similar kinetic fractionation is applied to diffusion during transport of gas phase CO_2 through the soil. The CO_2 diffusion module within ISOLSM is based on *Tans* [1998] and described in detail in *Riley et al.* [2002] and *Riley* [2005]. Similarly, the isotopic kinetic fractionations during soil evaporation are dependent on near-surface turbulent intensity as well as the ratio of $H_2{}^{18}O$ diffusivity to H_2O diffusivity [*Mathieu and Bariac*, 1996].

[7] The model computes gross CO_2 leaf fluxes from the atmosphere-to-leaf, F_{al} (mol m^{-2} s^{-1}), and from leaf-to-atmosphere, F_{la}, as [*Ciais et al.*, 1997a]:

$$F_{\mathrm{al}} = \left(\frac{C_a}{C_a - C_i}\right) F_A \tag{2}$$

$$F_{\mathrm{la}} = \left(\frac{C_i}{C_a - C_i}\right) F_A \tag{3}$$

where C_i is the CO_2 concentration inside the stomatal pores. The $CO^{18}O$ fluxes from leaves are calculated as follows:

$$^{18}F_{\mathrm{la}} = \alpha_l R_l F_{\mathrm{la}} \tag{4}$$

where α_l is the diffusive fractionation factor across the laminar leaf boundary layer and through the stomata, and R_l is the $CO^{18}O$ to CO_2 ratio within the leaves after equilibration with leaf water. The value of α_l is a weighted mean of fractionation factors for diffusion in the stomata, through the mesophyll cell wall, and through the laminar boundary layer and into the air space above the canopy. Note that this simplified estimates does not factor in recent findings of the strong kinetic effect from canopy-scale turbulent diffusion [*Lee et al.*, 2009]. The nonleaf CO_2 and $CO^{18}O$ respiration fluxes (F_r and $^{18}F_r$, respectively) are calculated as the sum of microbial, growth, and root and stem maintenance respiration.

[8] Detailed in *Still et al.* [2009], previous studies have tested ISOLSM simulations at the site level. These include studies that have validated ISOLSM's predictions of H_2O and CO_2 fluxes at different locations and different ecosystems [*Suyker and Verma*, 2001; *Riley et al.*, 2003; *Cooley et al.*, 2005; *Lai et al.*, 2006; *Aranibar et al.*, 2006; *Still et al.*, 2009]. ISOLSM's isotopic predictions have also been validated; comparing observed and simulated $\delta^{18}O$ values of ecosystem water pools and ecosystem H_2O and CO_2 fluxes throughout the Great Plains [*Riley et al.*, 2003; *Still et al.*, 2005; *Still et al.*, 2009; *Lai et al.*, 2006].

[9] ISOLSM simulations were forced with two sets of meteorological data: radiation, precipitation, height, wind speed, and sea-level and surface pressure from data generated by *Qian et al.* [2006]; and temperature and relative humidity from the Global Summary of the Day, which was obtained through the World Meteorological Organization and the National Climatic Data Center Climate Services Branch. The *Qian et al.* [2006] data set merges data from station measurements, remote sensing, and model simulation, using different products for each variable. A method similar to the *Cressman* [1959] objective analysis was used to interpolate the station observations onto the model grid. Appendix C contains a brief description of this data set and a comparison with other gridded data to demonstrate why it was preferred. It is important to note that although the model is forced with two different data sources, both are constrained by observations that are subject to the same meteorological conditions. The $\delta^{18}O$ value of precipitation (δW_P) was prescribed from a data set described in detail by N. H. Buenning and D. C. Noone (An evaluation of annual mean and seasonal timing of local and non-local processes controlling the isotopic composition of precipitation from observations and comprehensive models, manuscript in preparation, 2014), which was constructed using a regression/Fourier transform approach and was constrained by global observations [*Isotope Hydrology Section*, 2006]. The isotopic composition of atmospheric vapor (δW_{AV}) was prescribed from the above δW_P using the offset between precipitation and vapor as modeled by the Melbourne University General Circulation Model [*Noone and Simmonds*, 2002]. The reasoning for these choices of δW_{AV} and δW_P are described in more detail in section 4.

2.2. Ocean and Anthropogenic Fluxes

[10] The global distribution of net CO_2 fluxes between the ocean and the marine atmosphere, F_o (mol m^{-2} s^{-1}), and sea-air CO_2 partial pressures, p_o and p_a (Pa), were taken from a data set produced by *Takahashi et al.* [2002] and *Gurney et al.* [2002]. However, the one-way CO_2 fluxes (atmosphere-to-ocean (F_{ao}) and ocean-to-atmosphere (F_{oa})) must be considered independently (like the leaf fluxes), as their isotopic compositions differ. To calculate the two one-way fluxes (equations (6) and (7)), the air-sea gas exchange coefficient, K_{ex}, was first calculated [*Ciais et al.*, 1997a] (equation (5)):

$$F_o = K_{ex}(p_o - p_a) \tag{5}$$

$$F_{ao} = K_{ex} p_a \tag{6}$$

$$F_{oa} = K_{ex} p_o \tag{7}$$

[11] The ocean-to-atmosphere $CO^{18}O$ flux (mol m^{-2} s^{-1}), $^{18}F_{oa}$, was calculated as follows:

$$^{18}F_{oa} = \alpha_w R_o F_{oa} \tag{8}$$

where R_o is the $^{18}O/^{16}O$ ratio of dissolved CO_2 and α_w is the fractionation associated with CO_2 crossing the air-sea interface, using the value *Vogel et al.* [1970] measured at 0°C of +0.8‰ ($\alpha_w = 1 + \varepsilon_w$, $\varepsilon_w = +0.8‰$). The ratio R_o was calculated as

$$R_o = \alpha_{eq}(T_s) R_{ow} \tag{9}$$

where α_{eq} is the temperature-dependent equilibrium fractionation factor, T_s is sea surface temperature, and R_{ow} is the $^{18}O/^{16}O$ ratio of ocean surface water. Using reconstructed sea surface temperatures, T_s, from the NOAA_ERSST_V3 (data provided by the NOAA/OAR/ESRL PSD) [*Smith et al.*, 2008], the value of $\alpha_{eq}(T_s)$ was calculated using equation (1). The values of R_{ow} were obtained via data compiled by *LeGrande and Schmidt* [2006]. This data set was constructed using local (rather than global) relationships between ocean water $\delta^{18}O$ values and salinity from 50 years worth of available data. *LeGrande and Schmidt* [2006] found that their gridded estimates performed well in general but found errors in the deep ocean, locations near sea-ice, and regions that exhibit large seasonality. These last two regions and areas where observational constraints were sparse will likely cause some bias in our modeling results.

[12] Emissions from fossil fuel combustion, F_f, were acquired from the data set produced by *Andres et al.* [1996]. Also included in the model were fluxes from biomass burning F_b, using the Global Fire Emissions Database version 2 (GFEDv2) [*Van der Werf et al.*, 2006]. This flux does not include regrowth, and as *Ciais et al.* [1997a] points out, the regrowth can likely be neglected because of the small magnitude relative to F_{la} and F_{al} and the gross flux has an almost trivial disequilibrium with the atmosphere. Both of the anthropogenic fluxes were assumed to have the isotopic ratio of atmospheric oxygen, R_{O2} (where $\delta_{O2} = -17‰$), which assumes no fractionation as CO_2 is sourced to the atmosphere. Thus, the $CO^{18}O$ fluxes from both fossil fuel emissions and biomass burning were calculated as

$$^{18}F_f = R_{O2} F_f \tag{10}$$

$$^{18}F_b = R_{O2} F_b \tag{11}$$

2.3. Atmospheric Transport Model (CAM)

[13] Atmospheric concentrations of CO_2 and $CO^{18}O$ were simulated using the NCAR Community Atmosphere Model (CAM) [*Collins et al.*, 2006]. Taking into account the processes of the terrestrial biosphere, the ocean, and the anthropogenic sources, the temporal changes of CO_2 and $CO^{18}O$ can be written as

$$\frac{dC_a}{dt} = \frac{1}{M_a}\left[F_{la} + F_r + F_{oa} + F_f + F_b - (F_{al} + F_{ao})\right] \tag{12}$$

$$\frac{d^{18}C_a}{dt} = \frac{1}{M_a}\left[{}^{18}F_{la} + {}^{18}F_r + {}^{18}F_{oa} + {}^{18}F_f + {}^{18}F_b - (\alpha_l F_{al} + \alpha_w F_{ao}) R_a\right] \tag{13}$$

where R_a is the instantaneous ratio of atmospheric $CO^{18}O$ to CO_2 ($^{18}C_a/C_a$) and M_a is a conversion factor (with units of

Table 1. List of the Experiment Names With a Brief Description

Experiment Name	Description
HYD20	Soil CO_2 hydration is increased by a factor of 20 globally
HYD300	Soil CO_2 hydration is increased by a factor of 300 globally
RH	Global relative humidity is increased by 3.3%
RHTROP	Relative humidity is increased by 3.3% between 20°S and 20°N
PREC	Reduced the prescribed $\delta^{18}O$ of precipitation by 3.2‰ globally
PRECTROP	Reduced the prescribed $\delta^{18}O$ of precipitation by 3.2‰ between 20°S and 20°N
WV	Reduced the prescribed $\delta^{18}O$ of atmospheric water vapor by 3.2‰ globally
WVTROP	Reduced the prescribed $\delta^{18}O$ of atmospheric water vapor by 3.2‰ between 20°S and 20°N
PRECWV	Reduced the prescribed $\delta^{18}O$ of precipitation and atmospheric water vapor by 3.2‰ globally
PRECWVTROP	Reduced the prescribed $\delta^{18}O$ of precipitation and atmospheric water vapor by 3.2‰ between 20°S and 20°N
LIGHT	Repartitioning 7.5% of the direct radiation to diffuse and a 4% reduction in global downwelling solar radiation
TEMP	Global temperatures are increased by 1 K
ASSIM	Global 3.6% increase in F_{la} and F_{al} without any change to F_r
RESP	Global 3.6% increase in F_r without any change to leaf fluxes

moles of air m^{-2}). While all fluxes in equation (12) were computed by either ISOLSM or calculated from data sets, the atmosphere-to-surface $CO^{18}O$ fluxes in equation (13) were dependent on R_a, and were thus calculated at every time step within the atmospheric transport model CAM. Specifically, by allowing the atmosphere to interact with the surface fluxes, a steady state δC_a can be found (i.e., simulated local annual mean δC_a stays relatively constant). Note that this interactive approach slightly differed with other δC_a models that solely used CO_2 fluxes from offline calculations (e.g., *Ciais et al.* [1997a, 1997b] and *Peylin et al.* [1999]). On the other hand, the model framework used here is not a complete fully coupled model used by *Cuntz et al.* [2003a, 2003b]. Nonetheless, to resolve the three-dimensional δC_a field, account needs to be made for the advection tied to the mass evolution on the left-hand side, a task for which CAM is well suited.

[14] ISOLSM simulations ran twice through the 1979–2004 period, to fully spin-up the model's deep soil layers. The 12 (January through December) monthly mean surface fluxes of CO_2 and $CO^{18}O$ were computed using the last 36 years of the simulation (i.e., the second cycle through the 1979–2004 period). Because ISOLSM does not have a dynamic coupling between carbon uptake and respiration, a correction was used to adjust the (nonleaf) respiratory fluxes so that the surface ecosystem CO_2 fluxes were close to being balanced for every grid point in a manner similar to *Denning et al.* [1996] and *Riley et al.* [2005] (i.e., a method similar to the so-called "R*" approach). Global respiration was slightly adjusted even further such that simulated CO_2 concentrations gradually rose at a rate consistent with observations during the 1990s (3.2 GtC yr^{-1}) [*Denman et al.*, 2007], implying a slight terrestrial uptake of CO_2. These fluxes and the fluxes described in section 2.2 were then used as input for CAM. Additional tracers were used in CAM to quantify the contribution of each surface-to-atmosphere flux to the simulated CO_2 and $CO^{18}O$ concentrations. CAM simulations ran for 30 years with the last 10 years used for the analysis of the steady state conditions.

2.4. Experiments

[15] Fourteen experiments were performed to compute the sensitivity of the climatological δC_a values to each of the quantities that influence the fluxes described by equations (12) and (13). The experiments aimed to evaluate separately the influence of soil CO_2 hydration, atmospheric relative humidity, isotope hydrology, light levels, temperature, and CO_2 flux partitioning on spatial δC_a variations. Table 1 gives a brief explanation of each experiment along with the experiment name, which is used hereafter. For comparison with *Wingate et al.* [2009], we conducted two similar experiments where soil CO_2 hydration rates were increased by factors of 20 and 300 (HYD20 and HYD300, respectively). Station observed relative humidity was shown [*Buenning et al.*, 2011] to gradually increase within the Asia Pacific and the Tropical Americas by an average of 3.3% from 1993 to 1997 (a similar increase was observed in central Europe, western North America, and Siberia), a brief interval of time where δC_a decreased at nearly every station [*Ishizawa et al.*, 2002; *Flanagan*, 2005]. As such, a sensitivity experiment was preformed that increased the prescribed relative humidity at each grid point by 3.3% units globally (RH) and only within the tropics (equatorward of 20°N and 20°S, RHTROP). Also, observations in the Asia Pacific and Tropical Americas show a 3.2‰ decrease in δW_p during the same 1993 to 1997 period, and precipitation data sets within these tropical regions depict an increase in precipitation that is consistent with the so-called amount effect (δW_p anticorrelates with precipitation) [*Buenning et al.*, 2011]. To examine the influence of isotope hydrology on δC_a, a global 3.2‰ reduction was applied to the prescribed $\delta^{18}O$ values of precipitation (PREC). To examine how much of the response was from the tropics, the region that dominates terrestrial CO_2 exchanges, another experiment was performed in which the reduction was only applied within the tropics (PRECTROP). The same specifications were applied to the $\delta^{18}O$ values of water vapor only (WV and WVTROP) and then to both $\delta^{18}O$ values of precipitation and water vapor (PRECWV and PRECWVTROP) to further disentangle the role of hydrological isotopic forcing on δC_a. To estimate the influence of light levels on δC_a, 7.5% of the prescribed direct radiation was repartitioned to diffuse radiation (a 15% total change), while the total radiation was lowered by 4% (denoted as LIGHT). The sizes of these anomalies were chosen to be comparable to those following the eruption of Mount Pinatubo, as inferred by *Robock* [2000] and *Gu et al.* [2003]. The eruption of Mount Pinatubo also affected global air temperatures, and the role of temperature changes on δC_a was evaluated through an experiment in which global surface air temperatures were increased by 1 K (TEMP). In the TEMP experiment, relative humidity was kept unchanged; thus, there was also a slight increase in specific humidity. To evaluate how a change to the assimilation/respiration partitioning may influence δC_a, an experiment was conducted where photosynthetic leaf fluxes were increased globally by 3.6% (offline from both ISOLSM and CAM) without any change to nonleaf respiration (ASSIM). Another experiment was conducted that increased nonleaf respiration globally by 3.6% without any change to photosynthetic leaf fluxes (RESP). *Buenning et al.* [2011] estimated the 3.6% increase by weighting radiation changes (from 1993 to

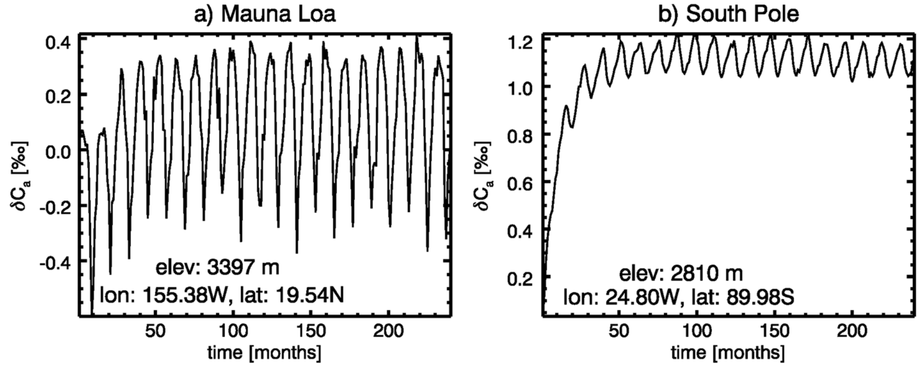

Figure 1. Time series of simulated δC_a at grid cells associated with the location of (a) Mauna Loa and (b) the South Pole. Each plot shows the first 20 years of the control simulation in CAM.

1997) within the tropics by predicted Net Primary Production from the Carnegie-Ames-Stanford Approach biosphere model [*Potter*, 1999; *Potter et al.*, 1999]. This estimate also takes into account the fraction of the tropics that contributes to global NPP.

3. Simulated CO$_2$ and CO^{18}O

[16] To facilitate later discussion and demonstrate model performance, the results from an unperturbed control simulation are presented first. Figure 1 shows model results for the first 20 years of the simulation at two grid cells associated with Mauna Loa (155.58°W, 19.54°N) and South Pole (24.80°W, 89.98°S). Modeled δC_a came to a quasi-steady state at about 5 years at these two locations (Figure 1). The time evolution of δC_a in Figure 1 demonstrates that treating the first 20 years of the simulation as spin-up is more than adequate. The global annual average quasi-steady state δC_a at the lowest level in the model (typically corresponding to a mean level of approximately 70 m above the Earth's surface) was found to be 0.48‰ (VPDB), which agrees reasonably well with the observed value of about 0.9‰ (e.g., NOAA/Global Monitoring Division data presented by *Cuntz et al.* [2003b]).

[17] Figure 2a shows observed and modeled (control simulation) zonal mean δC_a at the ground level as well as the contributions from the five components of the total surface-to-atmosphere flux. Both observed and simulated values of δC_a in Figure 2 were offset so that South Pole values equal 0‰, as is conventional in previous global model studies [*Ciais et al.*, 1997b; *Peylin et al.*, 1999; *Cuntz et al.*, 2002b; *Wingate et al.*, 2009]. Each station data point in Figure 2a was calculated by taking the mean of all monthly values (from the NOAA database) from 1990 to 2007; because not all stations started observations at the same time and have the same missing values, the station means will not span the same time intervals. The model simulated a north-south δC_a gradient that agrees well with observations, as is reflected in the high correlation coefficient in Figure 2a (r = 0.970; correlating 45 observed station annual means [*White and Vaughn*, 2009] with simulated values from the nearest grid cell). In general, these results suggest that the model's control simulation reasonably captured the north-south gradient of δC_a.

[18] It was found that forcing the model with δW_P data that were closely constrained by observations (N. H. Buenning and D. C. Noone, manuscript in preparation, 2013) was important for this successful model/data agreement. Previous runs of the model using simulated δW_P from models developed at Melbourne University (MUGCM) [*Noone and Simmonds*, 2002], the Max Planck Institute for Meteorology (ECHAM) [*Hoffmann et al.*, 1998], and the Goddard Institute for Space Studies (GISS) [*Jouzel et al.*, 1987] resulted in north-south

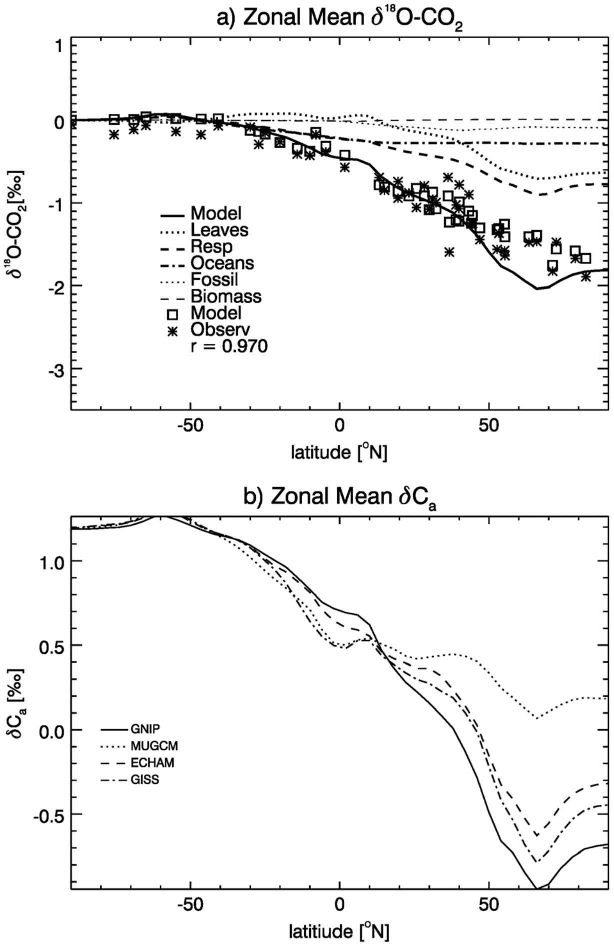

Figure 2. Simulated north-south gradient in δC_a (‰) (solid line) and the contributions from leaves (dark dotted), respiration (dark dashed), oceans (dash-dotted), fossil fuel emissions (light dotted), and biomass burning (light dashed). Asterisks represent an observed mean value, and the squares are from the closest grid cell to each observation. (a) The model's surface layer and (b) the modeled zonal mean for both all grid cells and the ocean points only are shown.

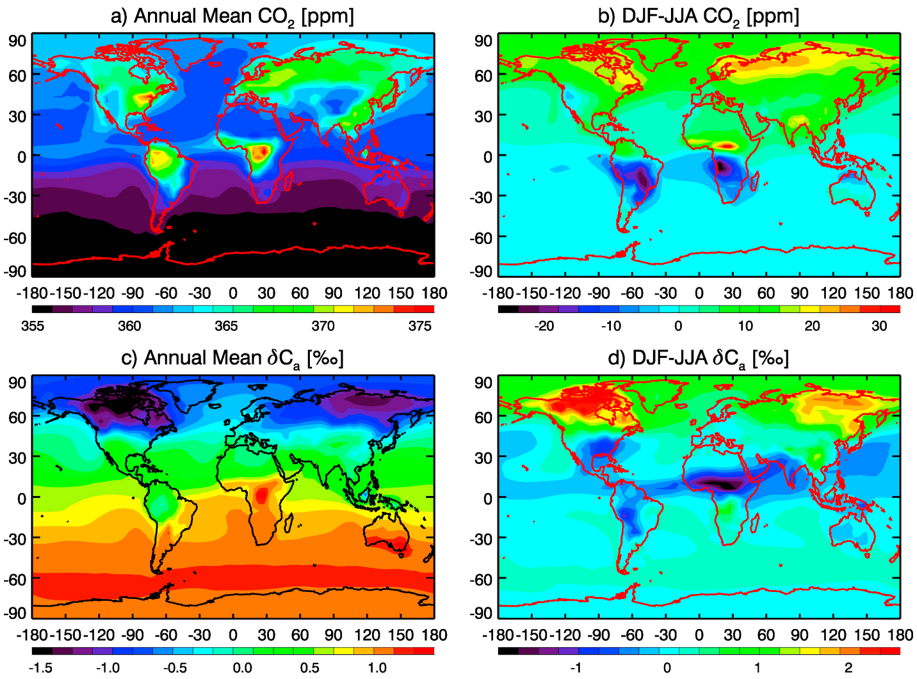

Figure 3. Simulated annual mean values of (a) CO$_2$ and (c) δC_a in units of ppm and ‰, respectively. The seasonal amplitude (i.e., the mean of December through February minus the mean of June through August) of (b) CO$_2$ and (d) δC_a are also shown.

δC_a gradients that were lower than what is observed (Figure 2b). Indeed, *Noone and Sturm* [2010] and N. H. Buenning and D. C. Noone (manuscript in preparation, 2013) report that these models underestimate the depletion of δW_P in parts of the northern middle and high latitudes, which caused the simulated gradients in δC_a to be too low.

[19] Additional tracers were implemented into CAM to quantify the contribution from each surface-to-atmosphere CO$_2$ flux, though the additional tracers are all subject to the same interactive atmosphere-to-surface fluxes (e.g., the fossil fuel tracer can be removed by atmosphere-to-leaf fluxes.). Unlike the results of *Cuntz et al.* [2002b], the model predictions implied very small contributions to the gradient from biomass burning and fossil fuel consumption likely due to differences in modeled global means (and therefore ecosystem isofluxes), and only about a 0.2‰ global contribution from ocean fluxes. Terrestrial ecosystem respiration contributed the most to the gradient, while leaf-to-atmosphere fluxes caused a stronger equator-pole gradient (i.e., not necessarily a pole-to-pole overall north-south gradient). This contribution from leaves was similar to the findings of *Cuntz et al.* [2002b] and contrasts with the model results of *Peylin et al.* [1999], whose low-latitude photosynthesis contribution to the equator-to-pole gradient was nearly canceled out by the contribution from high northern latitude photosynthesis. Because the isotopic composition of atmospheric vapor and precipitation are generally not depleted enough in GCMs (discussed above), it is likely that the discrepancy is due to differences in the isotopic composition of atmospheric vapor and precipitation, and thus more positive midlatitude and high-latitude leaf isofluxes to the atmosphere when forced with GCM water isotopologues.

[20] In agreement with a wide range of other transport modeling studies, the highest annual mean surface CO$_2$ concentrations for the control simulation were in the Northern Hemisphere, specifically over the northeastern United States and Eastern Europe (Figure 3a), a pattern that is consistent with a seasonal "rectifier effect" [*Denning et al.*, 1996]. These regions also had large differences in CO$_2$ concentrations between boreal winter (mean of December-January-February (DJF)) and summer (June-July-August (JJA)), with high CO$_2$ concentrations during the Northern Hemisphere winter when there was little photosynthetic activity (Figure 3b). Yet the largest difference between DJF and JJA were simulated over western tropical Africa, partially due to large seasonal variations in biomass burning.

[21] The $^{18}O/^{16}O$ composition of CO$_2$ (Figure 3c) was lowest over northern middle- to high-latitude forests where the $\delta^{18}O$ value of precipitation is relatively depleted and thus carbon fluxes deplete δC_a. These areas included the boreal forests of North America, Asia, and Eastern Europe. The high-latitude depletion is often characterized primarily as a result of the very negative soil respiration isoflux. However, if the $\delta^{18}O$ value of precipitation—and thus leaf water—is depleted enough, even leaf exchange fluxes can deplete the $^{18}O/^{16}O$ composition of back CO$_2$. As noted by *Still et al.* [2009], the isotopic composition of chloroplast CO$_2$ (δC_c) needs to exceed ~7‰ before the retro-diffused flux enriches δC_a. The simulations of *Ciais et al.* [1997b] showed high levels of depletion in the Northern Hemisphere's boreal forests, as well as in the Amazon, the Congo, and Southeast Asia, which were attributed to ecosystem fluxes; however, the simulations of *Cuntz et al.* [2003b] had only slightly depleted values over the Amazon, and to a lesser extent Southeast Asia with enriched values over the Congo. The simulated tropical δC_a shown here (Figure 3c) agrees better with the results of *Cuntz et al.* [2003b] than with *Ciais et al.* [1997b] with slight depletion over the Amazon and Southeast Asia and enrichment over the Congo.

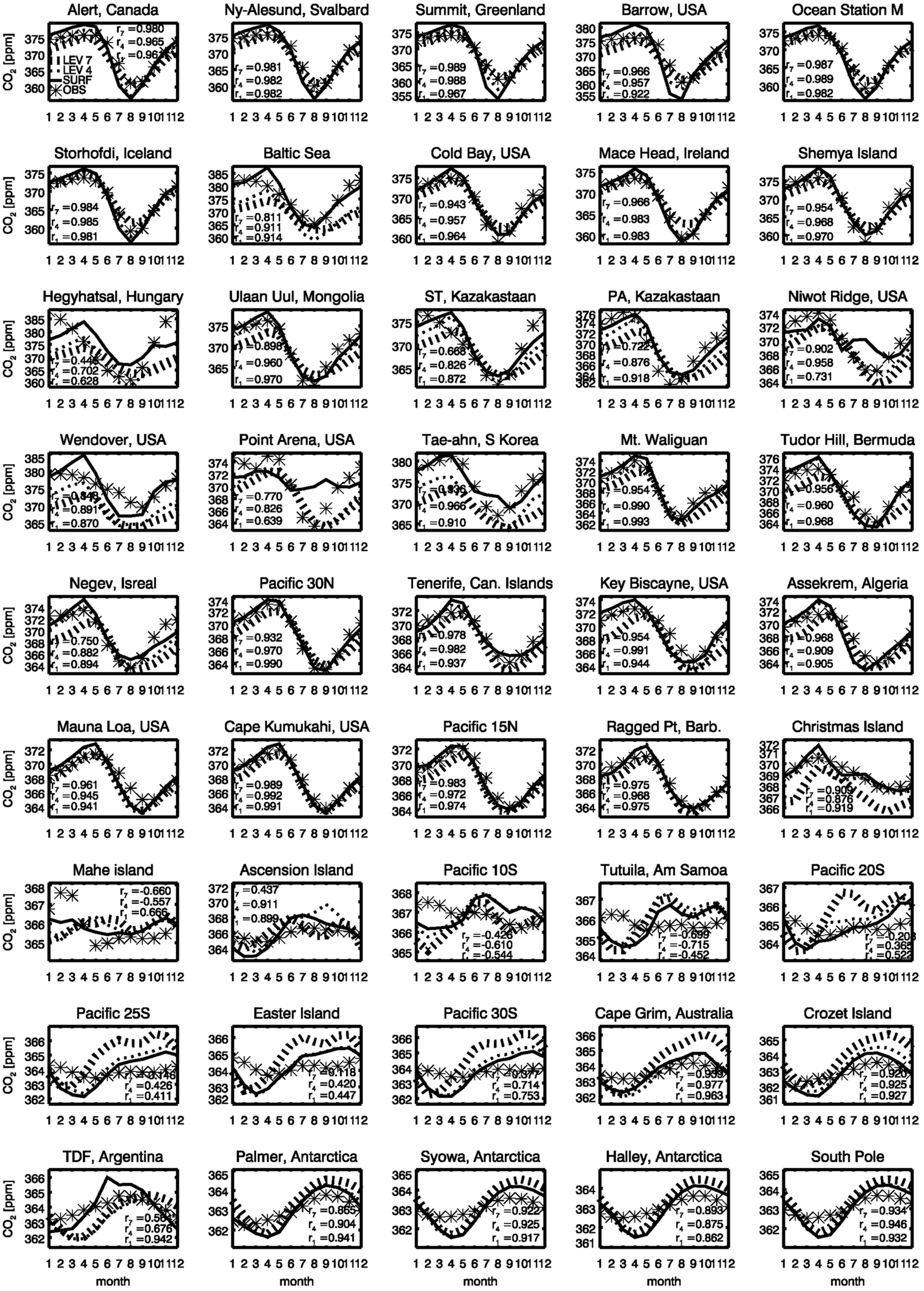

Figure 4. Observed seasonal cycles of CO_2 (ppm) for 20 stations around the world that have many observations on record (shown as asterisks). Solid lines are the simulated seasonal cycle at the model's surface level for the closest grid cell, while the dotted and dashed lines are the fourth and seventh model level, respectively.

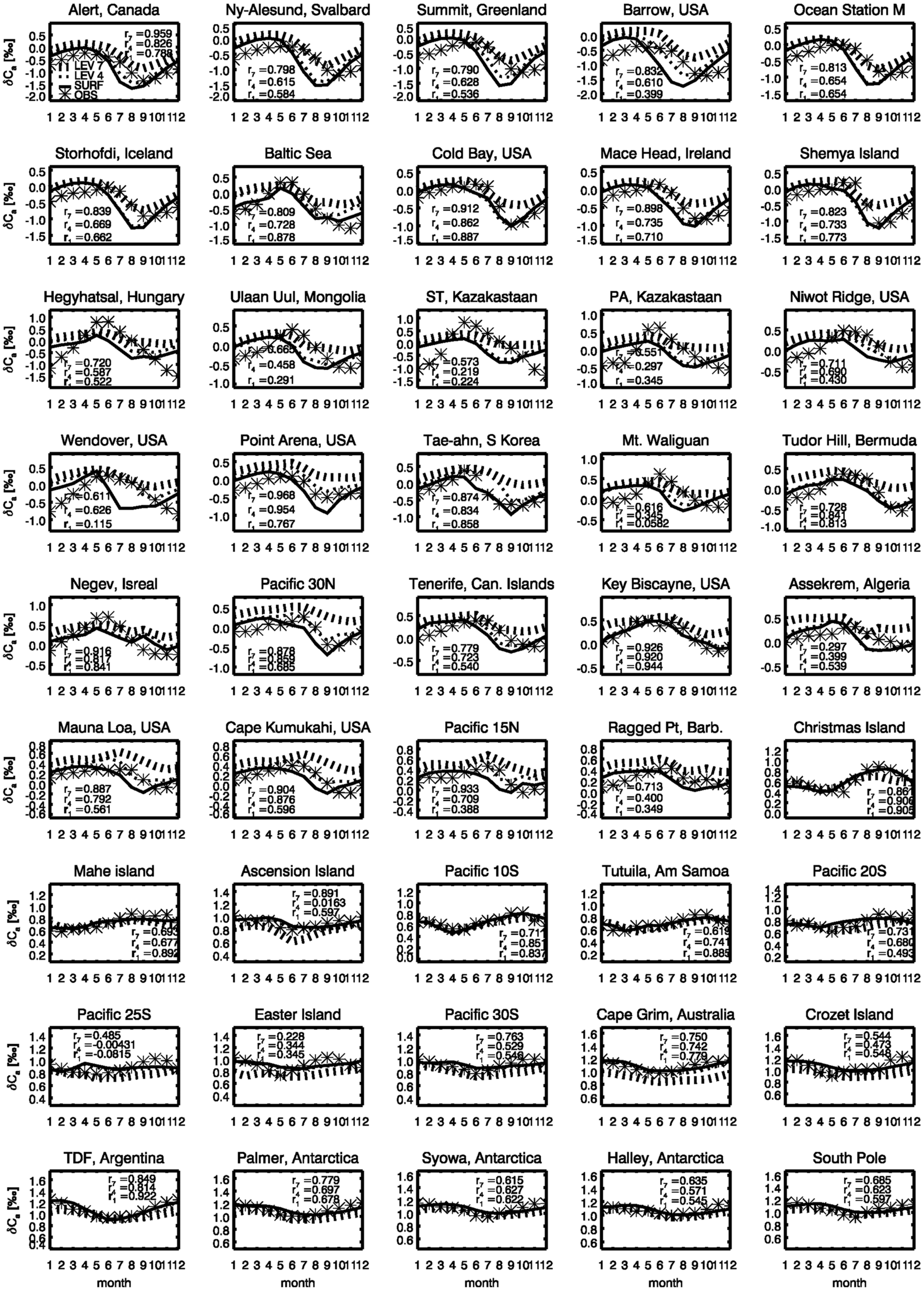
Alert, Canada; Ny-Alesund, Svalbard; Summit, Greenland; Barrow, USA; Ocean Station M; Storhofdi, Iceland; Baltic Sea; Cold Bay, USA; Mace Head, Ireland; Shemya Island; Hegyhatsal, Hungary; Ulaan Uul, Mongolia; ST, Kazakastaan; PA, Kazakastaan; Niwot Ridge, USA; Wendover, USA; Point Arena, USA; Tae-ahn, S Korea; Mt. Waliguan; Tudor Hill, Bermuda; Negev, Isreal; Pacific 30N; Tenerife, Can. Islands; Key Biscayne, USA; Assekrem, Algeria; Mauna Loa, USA; Cape Kumukahi, USA; Pacific 15N; Ragged Pt, Barb.; Christmas Island; Mahe island; Ascension Island; Pacific 10S; Tutuila, Am Samoa; Pacific 20S; Pacific 25S; Easter Island; Pacific 30S; Cape Grim, Australia; Crozet Island; TDF, Argentina; Palmer, Antarctica; Syowa, Antarctica; Halley, Antarctica; South Pole

Figure 5. Observed seasonal cycles of δC_a (‰) for 20 stations around the world (shown as asterisks). Solid lines are the simulated seasonal cycle at the model's surface level for the closest grid cell, while the dotted and dashed lines are the fourth and seventh model level, respectively.

[22] The DJF-JJA difference in δC_a (Figure 3d) was similar to that of CO_2 (Figure 3b) with large differences over some highly productive broadleaf forests like those in tropical Africa, and South America, as well over the northern boreal forests. The model also predicted the largest δC_a DJF-JJA differences in the high latitudes (especially in Canada and Russia), which was due to large seasonal variations in isotopically depleted ecosystem CO_2 fluxes. For instance, when ecosystem fluxes were highest over North America during June, July, and August, δC_a decreased locally because those fluxes acted to lower δC_a at middle and high latitudes. During winter months, ecosystem fluxes were depleted but very small, which allowed δC_a to slowly approach the global mean of δC_a via large-scale transport, thus causing large seasonal amplitudes.

[23] Simulated seasonal cycles of CO_2 and δC_a were compared to observed cycles at 45 NOAA sites [*White and Vaughn*, 2009] where there were the most δC_a observations for the 1990–2007 period (Figures 4 and 5). For each station, the 12 monthly means were calculated from each monthly value provided by the NOAA database. As with other studies [*Ramonet and Monfray*, 1996; *Cuntz et al.*, 2003b], some model grid cells have been shifted to take into account different sampling methods (e.g., Barrow and Cape Grim). It is also common for modeling studies to compare data from high elevation stations with model levels farther up in the atmosphere (e.g., Mauna Loa). Results from the lowest, fourth, and seventh model levels are shown in the figures to demonstrate the simulated seasonal cycles near the surface, the top of the boundary layer, and within the free troposphere, respectively. Model results away from the surface are also shown because many of the observing stations collect air samples when meteorological conditions favor a free atmosphere measurement (thus, limiting the influence of local fluxes). Making the comparison in this way is perhaps better at eliminating local effects than shifting to ocean grid cells, as seasonal changes in ocean fluxes in some regions can be large (e.g., summer ocean fluxes are high near Barrow but close to zero during the winter). To quantify the model's performance, correlation coefficients were calculated for the observed monthly means and the corresponding simulated monthly means at the model's surface, fourth, and seventh levels (corresponding to r_1, r_4, and r_7, respectively). These values are shown in Figures 4 and 5 for each station. Also, the seasonal range (maximum minus minimum) was computed at each station for both the observed and modeled values, and all model-observation differences are given in Tables D1 and D2. Similarly, the phase of the first harmonic (defined as the day of the seasonal maximum) of each seasonal time series was computed using Fourier transforms, and the first harmonic phase differences between model and observations are given in Tables D1 and D2. Furthermore, the CO_2 and δC_a model/observation differences are shown as a scatter plot in Figure 6 for both the amplitude and phase. It is important to note that the values given in Figures 4 and 5 and Tables D1 and D2 provide a quantification of the model's ability to predict the seasonal cycles, which is rarely done in global modeling studies of δC_a (though *Peylin et al.* [1999] calculated amplitude differences). These values can also serve as reference of comparison for future modeling studies.

[24] For the Northern Hemisphere stations, observed monthly CO_2 concentrations mostly fell on the curves derived from modeled surface values or in between the surface and the free atmosphere; thus, the model accurately captured the seasonal amplitude and phase of atmospheric CO_2. For example, at Cape Kumakahi, the seasonal cycle was modeled well at all three layers, as is reflected in the correlation coefficients (r_1, r_4, and r_7 equal 0.991, 0.991, and 0.989, respectively) and the low model-observation differences (Table D1). On the other hand, at Niwot Ridge, simulated amplitudes and phases matched up better with observations at the fourth and seventh levels (reflected in the r values and the differences in Table D1), as this station is at an elevation of 3475 m and the model did not resolve topography well for this region. Indeed, the fifth model level is the layer at which the average geopotential height is closest to the station's elevation. One model weakness found here was inaccurate simulation of CO_2 amplitudes in the Southern Hemisphere. An additional model simulation was performed where all ocean fluxes were set to zero, and the results suggest that the Southern Hemisphere CO_2 amplitude discrepancy was likely due to inaccurate ocean fluxes and not a problem with calculated land fluxes from ISOLSM. However, the large model amplitude near the tropics and Southern Ocean could also be due to inadequate transport within CAM, advecting too much CO_2 from the Northern Hemisphere into the Southern Hemisphere.

[25] Examining the simulated δC_a seasonal cycle (Figures 5 and 6 and Table D2) revealed that the simulated amplitude and phase at the lowest model level agreed well with observations at some stations (e.g., Baltic Sea and Cold Bay), while most stations agreed better with the fourth or seventh atmospheric layer (e.g., Alert, Barrow, and Mauna Loa), and others were not accurately predicted at any atmospheric layer, particularly continental stations that are likely influenced by a range of other surface properties and are less representative of free-troposphere values (e.g., Ulaan Uul, Wendover, and Mount Waliguan). There was also good agreement at stations in the Southern Hemisphere like the South Pole, Cape Grim, and American Samoa, locations where the seasonal cycle is primarily driven by shifts from Northern-to-Southern Hemisphere CO_2. The agreements in δC_a at these stations and the model's inaccurate CO_2 amplitudes at the same locations might indicate possible shortcomings in the spatial distribution of net exchanges with either the ocean or land ecosystems. Alternatively, at Barrow and Alert, the modeled surface amplitude was too large and the phase led the observations by about 2 months (63.5 days for Barrow) when comparing with the model surface level, although there was much better agreement at higher levels in the atmosphere (30.3 days). Figure 6 shows that the model predicts too large of a seasonal amplitude in both CO_2 and δC_a near the surface at the high northern latitude stations (red points on Figure 6a), a possible indication that the summer drawdown is too large in the high latitudes, which would also over-deplete atmospheric CO_2 in ^{18}O. The values in Table D2 reveal that in general, the model led observations at northern middle- and high-latitude locations, a common model shortcoming in previous studies, while slightly lagged the observations in the high latitudes of the Southern Hemisphere. Conversely, the phase differences were smallest in the tropics and subtropics. Based on the correlation coefficients in Figure 5 and the amplitude and phase differences, the stations where the model performed the worst were at Mount Waliguan and Wendover, Utah, where both the amplitudes and phases were inaccurately simulated. It was found that the model better captured the seasonal cycle at

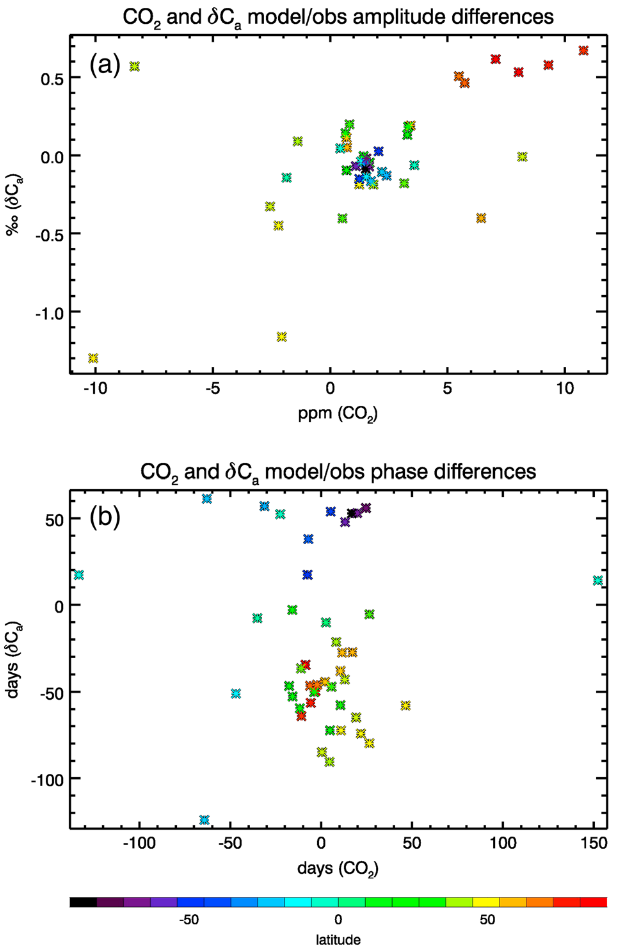

Figure 6. Scatterplots of seasonal cycle differences between model and observations at 45 stations with CO_2 plotted on the *x* axis and δC_a on the *y* axis. (a) The amplitude differences and (b) the phase differences are displayed.

these locations when comparing the observations with levels farther up in the atmosphere beyond the seventh level, which suggests that the model/observation mismatch is likely due to the model not resolving certain topographic features well for these mountainous regions. The mismatch could also be due to local fluxes that are unresolved in the model. However, there does not appear to be a clear relationship between phase differences in both δC_a and CO_2 (Figure 6b). The modeling of the δC_a seasonal cycle remains a challenge in the modeling community as this study and others [*Ciais et al.*, 1997b; *Peylin et al.*, 1999; *Cuntz et al.*, 2003b; *Wingate et al.*, 2009] have failed to demonstrate accurate modeling of the cycle at every location around the world, particularly the phase at high-latitude stations. Because the model best predicted the global mean and north-south gradient of δC_a, the sensitivity of the δC_a seasonal cycle is only briefly discussed in section 5.

[26] Validation of the control simulation provides some assurance that sensitivity calculations are meaningful; however, as in all modeling studies, we are cautious not to overstate the accuracy of any particular prediction. We have shown that many of the basic features of the CO_2 and δC_a climatology were well captured by this model. Nonetheless, no model is perfect, and one can certainly identify shortcomings in the reproduction of the existing observations. To minimize the influence of model shortcomings in our findings, the model experiments were designed to test the robustness of the mechanistic calculations that underpin the computed CO_2 and $CO^{18}O$ fluxes, while atmospheric transport accounts for the nonlocal influences of those fluxes. *Buenning et al.* [2011] argued that this type of approach was required to compliment observational work that can only provide limited assessment of mechanisms. As such, the focus of the model experimental results are on large-scale δC_a features, rather than on regional or local changes, since the modeled circulation is more reliable on large spatial scales, as demonstrated in the relatively accurate predicted mean and north-south gradient of δC_a.

4. Sensitivity of δC_a

4.1. Sensitivity to Soil CO_2 Hydration Rates

[27] The HYD20 and HYD300 simulations globally increased the soil CO_2 hydration rates at all locations. Like the experiments of *Wingate et al.* [2009], the increased hydration resulted in a decrease in the global mean δC_a

Table 2. Changes in the Global Annual Means of Transpiration (Q_V), Evaporation (Q_E), Photosynthesis (PSN), F_{la}, F_r, δW_l, δW_S, δF_{la}, δF_r, and δC_a

	Q_V[a]	Q_E[a]	PSN[a]	F_{la}[a]	F_r[a]	δW_l[b,c]	δW_S[b,d]	δF_{la}[b]	δF_r[b]	δC_a[b]
HYD20	-	-	-	-	-	-	-	0	−0.71	−0.15
HYD300	-	-	-	-	-	-	-	0	−1.3	−0.28
RH	−3.6	−2.9	2.7	4.2	2.3	−0.38	−0.081	−0.33	−0.096	−0.21
RHTROP	−2.4	−1.1	1.3	1.9	1.1	−0.14	0.0019	−0.10	−0.0029	−0.073
PREC	-	-	-	-	-	−2.1	−3.0	−1.8	−3.8	−1.8
WV	-	-	-	-	-	−1.4	−0.041	−1.3	−0.054	−0.78
PRECWV	-	-	-	-	-	−3.5	−3.0	−3.2	−3.9	−2.6
PRECTROP	-	-	-	-	-	−1.0	−0.79	−0.89	−1.9	−0.92
WVTROP	-	-	-	-	-	−0.67	−0.0011	−0.64	−0.0048	−0.37
PRECWVTROP	-	-	-	-	-	−1.7	−0.79	−1.5	−1.9	−1.3
TEMP	0.89	−0.63	0.25	−1.8	−0.44	−0.19	−0.069	−0.22	−0.17	−0.16
LIGHT	−0.059	−1.6	3.0	4.4	2.8	−0.19	−0.10	−0.16	0.019	−0.048
ASSIM	-	-	3.6	3.6	-	-	-	-	-	0.10
RESP	-	-	-	-	3.6	-	-	-	-	−0.10

[a] Units are in %.
[b] Units are in ‰.
[c] Weighted by photosynthesis.
[d] Weighted by respiration.

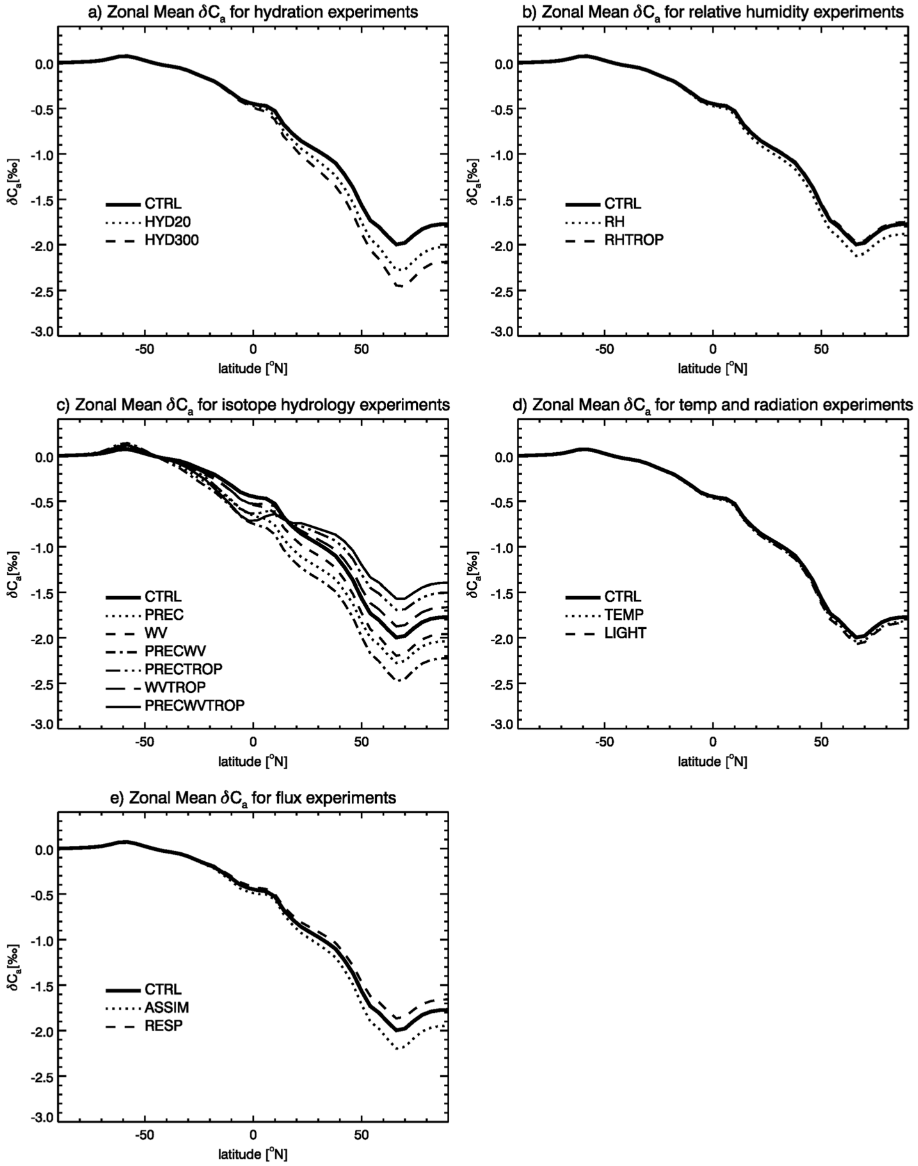

Figure 7. Zonal and annual mean δC_a (‰) for (a) the soil hydration, (b) relative humidity, (c) isotope hydrology, (d) temperature and radiation, and (e) CO_2 ecosystem fluxes model sensitivity experiments. Each panel compares the respective model experiments with the control simulation (CTRL).

(Table 2) and an increase in the north-south δC_a gradient (Figure 7a). The decrease in global mean δC_a due to increased hydration rates was a result of the invasion flux being accounted for in ISOLSM [*Riley et al.*, 2003; *Riley* 2005]; this explanation is consistent with that reported by *Wingate et al.* [2009].

[28] The north-south δC_a gradient increased by 0.29‰ and 0.48‰ for the HYD20 and HYD300 experiments, respectively, which agrees well with the results of *Wingate et al.* [2009]. Figure 8 shows that the largest change in δC_a for the two experiments occurred in high northern latitudes. The largest change to annual mean δC_a occurred over northern Siberia, where soil water δ^{18}O values were especially depleted [*Ciais et al.*, 1997a]. Despite the simulated increase in the north-south gradient in δC_a found here, the experiments did not result in a better agreement with the observations in both the global mean (0.68‰ too low for HYD300) and the north-south gradient (0.58‰ too steep for HYD300), as it did in *Wingate et al.* [2009]. Additionally, there is very little observational basis for such increased soil CO_2 hydration rates across a range of ecosystems. And, as was shown by *Riley et al.* [2002] and *Riley* [2005], increasing soil hydration rates in those ecosystems with sharp gradients in upper soil water isotopic composition from evaporation can also enrich δC_a. In the following subsections, we show that the modeled north-south gradient is also sensitive to other variables that affect the δC_a budget and not considered by *Wingate et al.* [2009].

4.2. Sensitivity to Relative Humidity

[29] Transpiration is driven by the diffusion of vapor from leaves, and that rate is driven by the difference between the vapor pressure in the interior of plant leaves and the vapor pressure of the surrounding air. As such, transpiration (and latent heat exchange in general) is expected to change when

a) Change in δC_a [‰]: HYD20-CTRL

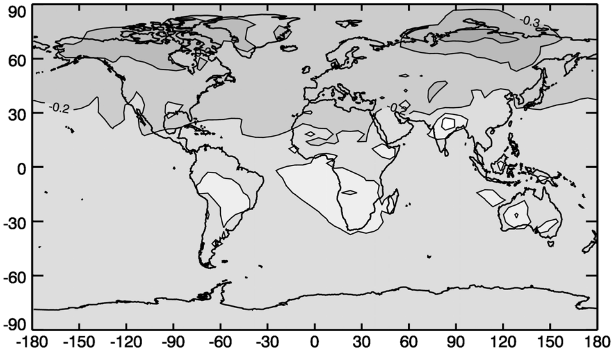

b) Change in δC_a [‰]: HYD300-CTRL

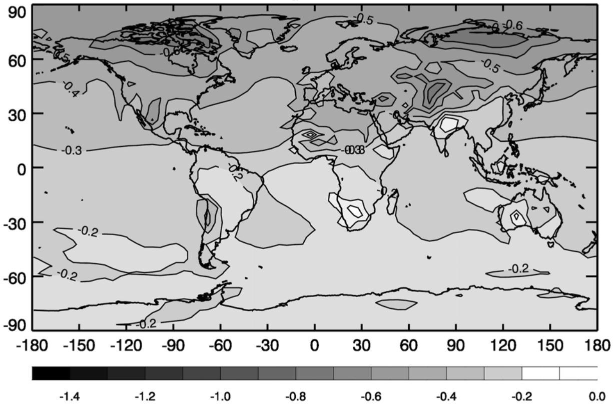

Figure 8. Global distribution of the change in annual mean δC_a (‰) for the (a) HYD20 and (b) HYD300 experiments. Contour intervals are 0.1‰, which is different than Figures 9, 11, and 13.

atmospheric relative humidity increases, as has been seen in observations during the mid-1990s for some high-flux regions [*Buenning et al.*, 2011]. Indeed, when relative humidity was increased by 3.3% (on an absolute basis), the global mean transpiration decreased by 3.6% (Table 2) due to a decrease in the vapor pressure gradient.

[30] A similar result was found for soil water where increased humidity caused a 2.9% reduction in evaporation and a slight increase (1.4%) in soil moisture. These changes in latent heat fluxes likely caused a change to the $CO^{18}O$ isoflux to the atmosphere from the leaves (I_{la}) and respiration (I_r), which can be quantified by:

$$I_{\mathrm{la}} = F_{\mathrm{la}}(\delta F_{\mathrm{la}} - \delta C_a) \tag{14}$$

$$I_r = F_r(\delta F_r - \delta C_a) \tag{15}$$

[31] It can be seen from equations (14) and (15) that the isofluxes are dependent on both the magnitude and the isotopic composition of the fluxes, δF_{la} and δF_r (note that both δF values factor in kinetic fractionation). Because the isotopic composition of the flux is strongly related to the isotopic composition of leaf and soil water, changes to δW_l and δW_S are first evaluated, followed by an assessment of changes from leaf and respiration fluxes (F_{la} and F_r).

[32] The predicted decrease in transpiration from increased relative humidity is consistent with an effective reduction in kinetic fractionation (equation (B4)). This change reduced leaf water ^{18}O enrichment, resulting in a reduced enrichment of the CO_2 molecules in equilibration within the stomatal cavity. The global changes in the isotopic compositions of leaf and soil water following a 3.3% absolute increase in relative humidity were −0.38‰ and −0.081‰, respectively. Differentiating equation (B4) with respect to humidity gives an upper limit to the expected relationship between leaf water $^{18}O/^{16}O$ content and humidity; for typical values of δW_X, δW_{CV}, and the fractionation coefficients, $\partial \delta W_{l\text{-CG}}/\partial h_l \approx -0.36‰\ \%^{-1}$. ISOLSM predicted that the 3.3% increase in relative humidity only caused a 2.0% increase in photosynthesis-weighted h_l. This change in h_l caused a global reduction in photosynthesis-weighted δW_l to be slightly over half the theoretical value expected from the *Craig and Gordon* [1965] steady state model. This difference was partially due to the fact that ISOLSM used the time-dependent leaf water model rather than the steady state model, and partially due to the inclusion of leaf boundary layer effects [*Still et al.*, 2009]. The nonsteady state model reduced the diurnal amplitude of leaf water enrichment and in particular restricted the otherwise extreme enrichment during early afternoon.

[33] Predicted changes in leaf and soil CO_2 fluxes are shown in Table 2. The increase in relative humidity caused a global increase in predicted assimilation, which in turn increased the leaf-to-atmosphere flux globally by 4.2%, and thereby increased the isoflux to the atmosphere. However, this effect was partially balanced by the reduction in δF_{la}. The RH experiment also showed similar changes to the soil-respired CO_2 fluxes, which for many regions deplete δC_a. Growth respiration is related to both the leaf area index and assimilation, and because assimilation increased, growth respiration also increased, which led to an overall increase in total ecosystem respiration. For regions where soil respiration depletes δC_a values, the combination of more depleted soil water (and thus decreased δF_r) and increased respiration both acted to increase the depleting isoflux, I_r. Thus, it was not clear if the changes to leaf fluxes caused δC_a to go up or down from equation (14) alone, though the changes to respiratory fluxes should in all cases cause δC_a to decline (through equation (15)), which highlights the need to use a fairly comprehensive land surface model like ISOLSM.

[34] The RH experiment (where relative humidity was increased by 3.3% globally) depleted δC_a by 0.21‰. Results from RHTROP (where relative humidity was increased by 3.3% only within the tropics) suggest that 0.073‰ of this response was from the tropics (Table 2), an indication that δC_a is more sensitive to relative humidity in regions outside of the tropics. This was at least partly due to the uniformly high relative humidity found in most tropical areas: At high humidity, δW_l is dominated by atmospheric water vapor isotopic composition and equilibrium fractionation effects, similar to the extreme case noted in Appendix B with 100% relative humidity. By contrast, in extratropical regions where relative humidity is often below 50%, the impact of soil source water and kinetic isotope effects are more important for δW_l, and thus increases in relative humidity in these regions might have larger impacts. Additionally, because δF_{la} and δF_r are close to background δC_a, tropical isofluxes are smaller than would be expected based on CO_2 fluxes. If one were to estimate the global mean change in δC_a due to changes in leaf water enrichment by means of the budget equation used by *Buenning et al.* [2011] for the RH experiment (with their

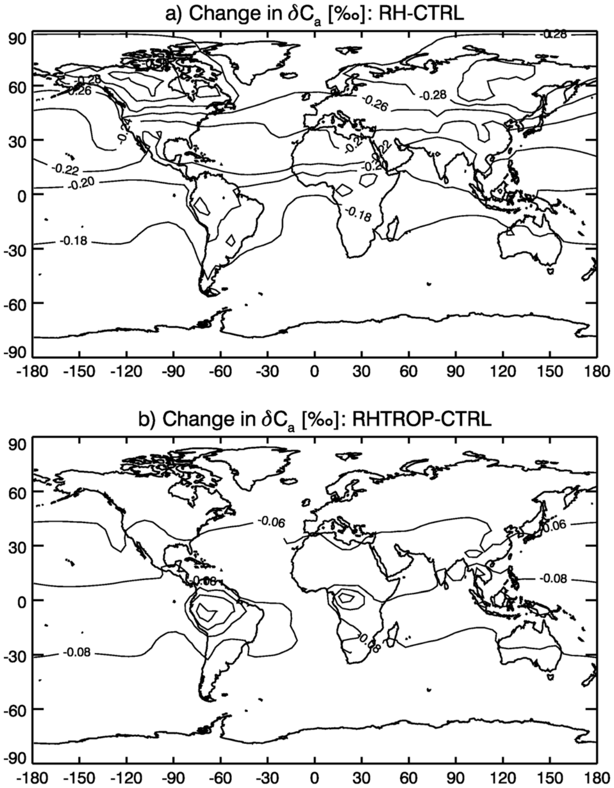

Figure 9. Global distribution of the change in annual mean δC_a (‰) for the (a) RH and (b) RHTROP experiments. Contour intervals are 0.02‰, which is a different interval than Figures 8 and 10.

equation applied globally), the estimated change in δC_a would be -0.63‰. This comparison indicates that feedbacks, atmospheric transport, and changes to CO_2 fluxes counteracted the expected changes due to decreased δW_l alone.

[35] The RH experiment increased the north-south δC_a gradient by 0.13‰, while the RHTROP slightly decreased the gradient by 0.023‰ (Figure 7b). When the humidity was changed globally, the largest decrease to δC_a occurred over northern Canada and Siberia (Figure 9a). When the relative humidity anomaly was only applied to the tropics, the change in δC_a over the northern regions was relatively small (Figure 9b). Northern Canada and Siberia have strong negative isofluxes from both leaf and soil fluxes, and the relative humidity increase not only further depleted the isotopic composition of these fluxes but also increased the fluxes themselves. This response was not the case for regions within the subtropics and parts of the middle latitudes where leaf fluxes do not always deplete the atmosphere of $CO^{18}O$. These results suggest that the north-south δC_a gradient can be increased by global increases in relative humidity, and one might expect the change to be greater if relative humidity were only to rise in the middle and high latitudes. These results suggest the possible use of the north-south δC_a gradient measurement as a sensitive proxy of flux-weighted relative humidity changes in midlatitude and high-latitude regions of the Northern Hemisphere. For instance, *Buenning et al.* [2011] showed how relative humidity increased during the mid-1990s throughout most of central Europe, a broad region of Siberia, and most of western North America. This would have caused an increase in the north-south gradient; however, relative humidity also increased in the Tropical Americas and the Asia Pacific during the mid-1990s, which likely outweighed the midlatitude change.

4.3. Sensitivity to $\delta^{18}O$ Values of Precipitation and Water Vapor

[36] The isotopic composition of leaf and soil water depends principally on the $\delta^{18}O$ values of precipitation and atmospheric water vapor (δW_P and δW_{AV}), along with kinetic and equilibrium fractionation factors. The soil water $^{18}O/^{16}O$ content should be closely linked with δW_P, and also with δW_{AV} in upper soil layers subject to evaporation. The value of δW_l depends on the $\delta^{18}O$ values of soil water (via root uptake without fractionation; equation (B4)) and on the $\delta^{18}O$ values of canopy vapor. Therefore, it is hypothesized here that decreases in δW_P will reduce both δW_l and δW_S, which would ultimately reduce δC_a.

[37] As described in section 2.4, two experiments were constructed to examine the effects of changes in δW_P independent of changes in δW_{AV}: (1) an overall 3.2‰ decrease in δW_P (PREC) and (2) a 3.2‰ decrease in δW_P in only the tropics (PRECTROP). The reduction of δW_P by 3.2‰ caused δW_l and δW_S to decrease globally by 2.1‰ and 2.7‰, respectively (Table 2). Results from the PRECTROP simulation revealed that the tropics contributed about half of the change in photosynthesis-weighted δW_l (i.e., the tropics made up about half of global photosynthesis in our simulation).

[38] To examine the impact of the $\delta^{18}O$ value of atmospheric water vapor (δW_{AV})—independent of changes in δW_P—on the isotopic composition of leaf and soil water, the same perturbations were applied to δW_{AV}. Lowering δW_{AV} by 3.2‰ (WV) caused a global decrease in δW_l and root-weighted δW_S of 1.4‰ and 0.065‰, respectively. When the change was only applied to the tropics, there was approximately no change to the global mean δW_S and a decrease in δW_l of 0.67‰. These results suggest that δW_l is sensitive to changes in the isotopic composition of atmospheric vapor as implied by equation (B4), though soil water is not. Not surprisingly, these simulations revealed that δW_S is mostly dependent on the isotopic composition of precipitation, but δW_l depends on both the isotopic composition of precipitation and vapor. However, it should be noted that these dependencies are partially a result of the equations used in ISOLSM (e.g., *Riley et al.* [2002, equation (20)]).

[39] In the PRECWV simulation, where δW_P and δW_{AV} were both reduced by 3.2‰, the isotopic composition of root-weighted soil water decreased by only 3.0‰. The small discrepancy between the perturbation and the response was a result of bottom layer recharge when the soil column dried out. In the model, the recharged water carries the same isotopic composition of the bottom soil layer, so the recharge of bottom layer water was only indirectly affected by the isotopic forcing. The isotopic composition of soil water becomes even less dependent on precipitation if the rate of recharge is greater than the infiltration rate. Results from the PRECWVTROP simulation showed that 1.7‰ of the change in δW_l came from the tropics, which again was a consequence of about half of global photosynthesis coming from the tropics.

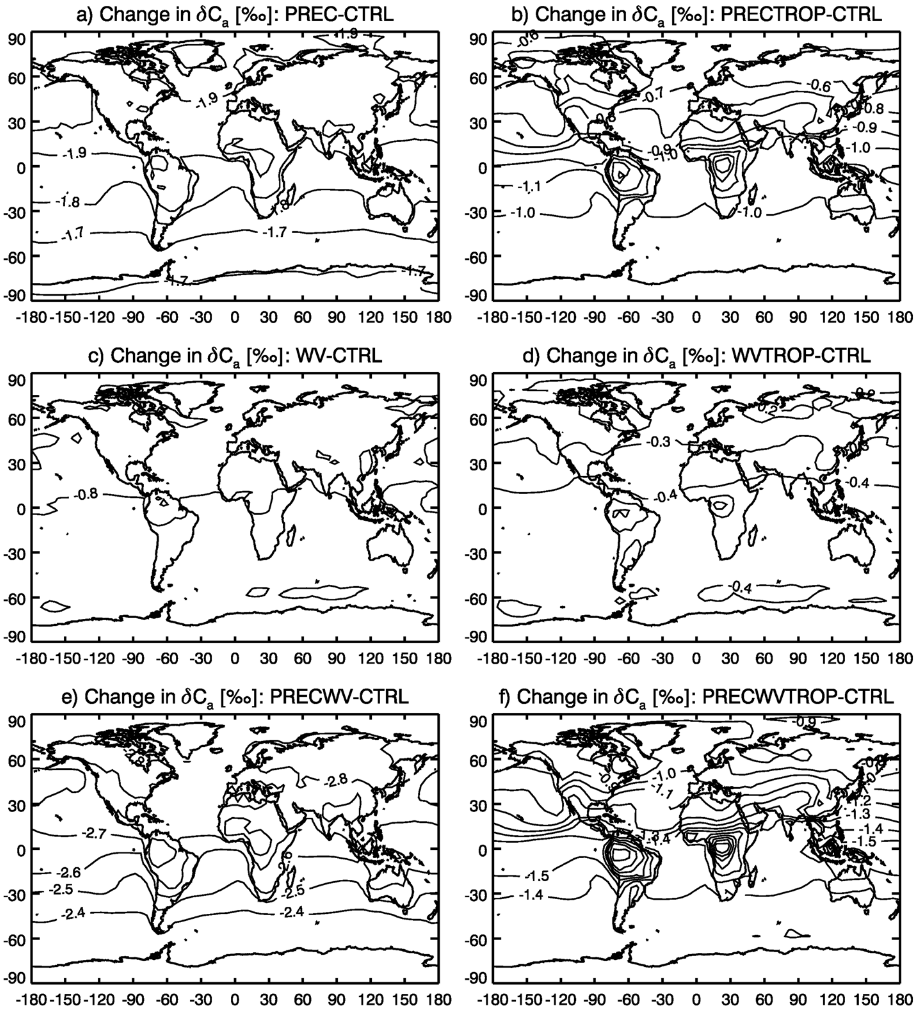

Figure 10. Global distribution of the change in annual mean δC_a (‰) for the (a) PREC, (b) PRECTROP, (c) WV, (d) WVTROP, (e) PRECWV, and (f) PRECWVTROP experiments. Contour intervals are 0.1‰, which is different than Figures 9, 11, and 13.

[40] The changes in the isotopic composition of ecosystem leaf and soil water pools induced similar changes to the isotopic composition of ecosystem CO$_2$ fluxes and subsequently of atmospheric CO$_2$ (Table 2 and Figure 10). For the experiments in which only the isotopic composition of precipitation was reduced (PREC and PRECTROP), global and annual mean δC_a decreased by 1.8‰ and 0.92‰, respectively. The reduction in δC_a was not as large when only δW_{AV} was decreased in the WV and WVTROP simulations (-0.78‰ and -0.37‰, respectively). When the isotopic composition of both precipitation and water vapor were reduced in the PRECWV and PRECWVTROP experiments, the model predicted the largest change to the global and annual mean δC_a (-2.6‰ and -1.3‰, respectively). It is not likely the changes to δW_P and δW_{AV} occurred globally; however, *Buenning et al.* [2011] highlighted three tropical stations (Bangkock, Darwin, and Izobamba) within the Global Network of Isotopes in Precipitation (GNIP) network that observed a decrease in δW_P during the mid-1990s (note that there were only five tropical GNIP stations that have more than 90 months of data on record from 1990 to 2005). *Welp et al.* [2011] showed that this decrease also occurred for a spectrally nudged simulation of the Isotope-incorporated Global Spectral Model (IsoGSM) [*Yoshimura et al.*, 2008]. Recall that this is the same time interval in which certain tropical and midlatitude regions observed an increase in relative humidity. Thus, it is possible that tropical changes to relative humidity, δW_P, and δW_{AV} drove a large fraction of the observed decrease in δC_a during the 1990s.

[41] The three globally perturbed experiments drove significant increases in the δC_a latitudinal gradient (Figure 7c). Indeed, the largest impacts to δC_a occurred over the continents, especially over northern Canada and Siberia (Figure 10). These results indicate that the north-south δC_a gradient is especially sensitive to global changes in the ^{18}O/^{16}O composition of both vapor and precipitation (without corresponding changes to the δW_p and δW_{AV} gradients, i.e., when all values are shifted to more negative values). On the other hand, when the offset was only applied to the tropics, the opposite effect occurred. Although the tropics-only experiments caused a decrease in δC_a at all latitudes (Table 2 and Figure 10), the largest decrease occurred in the Southern Hemisphere and within the tropics, thus decreasing the north-south δC_a gradient. We therefore conclude that the largest increase in the δC_a gradient will occur when δW_p and δW_{AV} decrease only in the northern middle and high latitudes.

a) Change in δC_a [‰]: LIGHT-CTRL

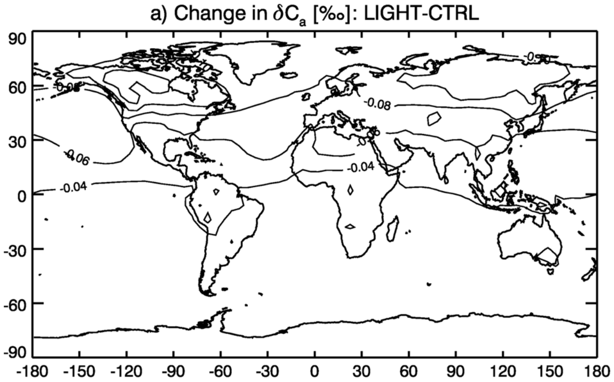

b) Change in δC_a [‰]: TEMP-CTRL

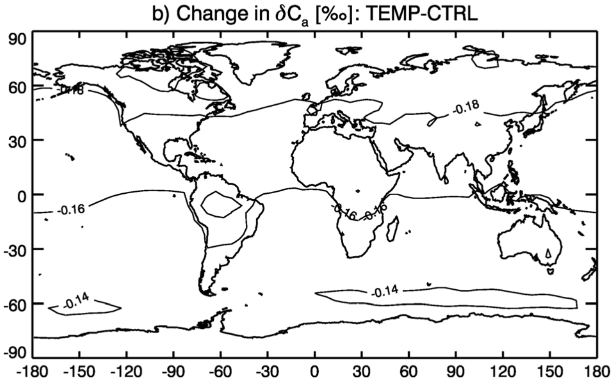

Figure 11. Global distribution of the change in annual mean δC_a (‰) for the (a) LIGHT and (b) TEMP experiments. Contour intervals are 0.02‰, which is different than Figures 8 and 10.

4.4. Sensitivity to Radiation

[42] The LIGHT experiment attempted to represent light levels following the eruption of Mount Pinatubo by reducing total downwelling solar radiation by 4% and repartitioning 7.5% of the direct light to diffuse light (15% total) [*Gu et al.*, 2003]. ISOLSM is well suited for this experiment, as it calculates both sunlit and shaded leaf photosynthesis, and shade leaf light use efficiency (LUE) is about 4 times greater than sunlit leaf LUE. Model predictions revealed that these combined radiation changes caused global mean transpiration to decrease by only 0.059%. Two additional simulations were conducted that imposed each light level change separately to better understand which change dominated the model response. Because diffuse light is able to reach the leaves deeper within the canopy, proportionally more evaporation from shade leaves can result, and thus, more diffuse light could drive an increase in ecosystem transpiration and photosynthesis when and where the leaf area index is high and midday light saturation occurs. On the other hand, the 4% reduction in total solar downwelling will cause decreases in leaf temperature and water evaporation from the mesophyll cells. Results from the additional experiments revealed that the 4% reduction caused global transpiration (mostly from sun leaves) to decrease by 1.85%, while the repartitioning from direct to diffuse radiation caused a 1.80% increase in transpiration. Thus, the two radiation changes opposed one another and resulted in a very small change in global average transpiration.

[43] The very small change in transpiration was not expected to greatly impact the isotopic composition of leaf water. However, photosynthesis-weighted δW_l was reduced globally by 0.19‰. About 0.1‰ of the change was due to a 0.3% global increase in photosynthesis-weighted values of h_l that resulted from the radiation changes. The other 0.09% was due to increases in photosynthesis, especially over the northern boreal forests where δW_l was low relative to the global mean. The 0.19‰ decrease in δW_l resulted in a 0.16‰ decrease in δF_{la}. The decrease in soil evaporation lowered δW_S by only 0.013‰, though the values of δF_r increased globally by 0.019‰. The difference in sign between these two isotopic changes was a result of a slight decrease in soil temperatures, which slightly increased the H_2O-CO_2 equilibrium fractionation (equation (1)).

[44] The light level changes only caused a 0.048‰ decrease in the global mean δC_a, which was a much smaller response compared to the relative humidity and isotope hydrology changes (Table 2). Not surprisingly, the north-south gradient also exhibited only a small change, a decrease of 0.073‰ (Figure 7d). Despite this small change, δC_a was most sensitive to radiation changes in the interior of northern Canada and northern Asia (Figure 11a), the same regions where relative humidity and isotope hydrology changes caused the largest δC_a response. These responses (and the responses discussed in the previous two subsections) occurred because δF_{la} was lowest for these two northern regions (Figure 12), and thus had the most negative isoflux from leaves (equation (14)) of any continental regions (i.e., had the largest impact on δC_a). Any decrease to δF_{la} (as occurred in the global sensitivity experiments shown here) will cause the leaf retro-diffused isoflux to be even more negative and further drive down regional δC_a. On the other hand, certain locations in the tropics and subtropics have δF_{la} that are higher than δC_a; thus, lowering δF_{la} would bring the leaf-to-atmosphere isoflux closer to zero (though the atmosphere-to-leaf component will always be positive).

4.5. Sensitivity to Temperature

[45] Temperature influences the isotopic composition of leaf and soil water—and eventually that of CO_2—partially through its impact on equilibrium fractionation [*Majoube*, 1971]:

$$\varepsilon_{LV}(T) = \exp\left(\frac{1137}{T^2} - \frac{0.4156}{T} - 0.0020667\right) - 1 \qquad (16)$$

δF_{la} [‰] Control Simulation

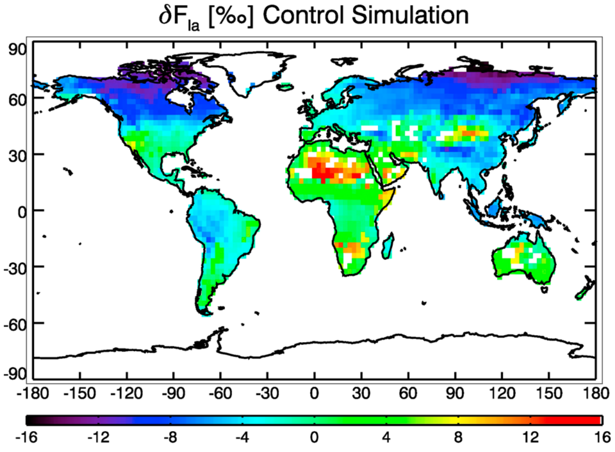

Figure 12. Global distribution of annual mean δF_{la} (‰) for the control simulation.

a) Change in δC_a [‰]: ASSIM-CTRL

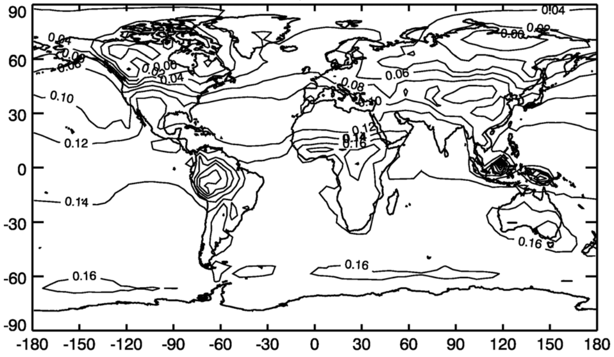

b) Change in δC_a [‰]: RESP-CTRL

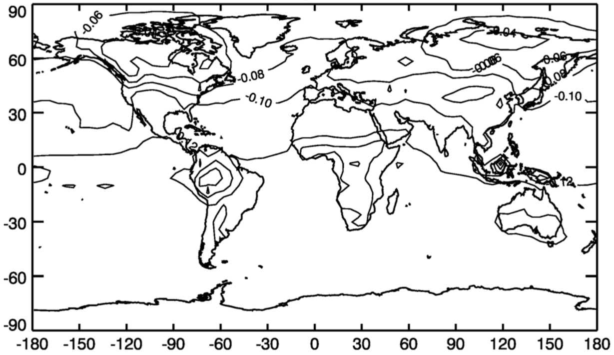

Figure 13. Global distribution of the change in annual mean δC_a (‰) for the (a) ASSIM and (b) RESP experiments. Contour intervals are 0.02‰, which is different than Figures 8 and 10.

[46] Differentiating equation (16) with respect to temperature results in a sensitivity of $d\varepsilon_{LV}/dT = -0.099‰\ K^{-1}$ at 280 K. Furthermore, in the middle and high latitudes, temperature can also constrain ecosystem fluxes [*Nemani et al.*, 2003]. Thus, temperature influences both the isotopic composition and the magnitude of the CO_2 and H_2O fluxes (in often counteracting ways).

[47] Results from the TEMP experiment, in which global surface air temperatures were increased by 1 K, showed a change in global transpiration and soil evaporation of 0.89% and −0.63%, respectively; implying that the air temperature increase only slightly modified the partitioning of latent heat components (note that this experiment did not alter atmospheric relative humidity). δW_S decreased globally by 0.055‰, which was less than the theoretical sensitivity based on equilibrium fractionation. Photosynthesis-weighted δW_l decreased globally by 0.19‰. By calculating the global means of other variables (such as relative humidity and surface temperature), it was determined that 0.014‰ of the decrease was due to the decrease in δW_S, 0.088‰ from the change of ε_{LV} in equation (B4), 0.010‰ from changes to photosynthesis, and about 0.055‰ due to a slightly increased relative humidity at the surface of the leaf.

[48] Temperature-dependent equilibrium fractionation also takes place as CO_2 interacts with leaf and soil water [*Ciais et al.*, 1997a], with a temperature sensitivity of $d\varepsilon_{eq}/dT = -0.22‰\ K^{-1}$ at 280 K (recall that $\varepsilon_{eq} = (\alpha_{eq} - 1) \times 1000$). Both δF_{la} and δF_r decreased more than the isotopic composition of leaf and soil water, which was a result of the reduction in equilibrium CO_2-H_2O fractionation due to increased ground and leaf temperatures (both of which increased globally by about 0.89 K). The global mean δC_a decreased by 0.16‰ (Table 2), and the north-south δC_a gradient increased by only 0.054‰ (Figure 7e). As in the other experiments, the largest response was in the northern parts of Canada and Asia where the negative isoflux in the control simulation was the greatest (Figure 11b). These results indicate that the influence of changes in temperature on the isotopic composition of leaf and soil water, and thereby on the isotopic composition of ecosystem fluxes, can affect the global mean of δC_a, though it has little effect on the north-south δC_a gradient.

4.6. Sensitivity to Assimilation/Respiration Partitioning

[49] δC_a is commonly thought of as a tracer of the partitioning between assimilation and respiration. In the ASSIM experiment, assimilation was increased globally by 3.6% (an estimate used by *Buenning et al.* [2011]), while nonleaf respiration fluxes were held unchanged relative to the control simulation. Thus, there was no change to the isotopic composition of the fluxes for this experiment, simply a change in the balance between assimilation and respiration. It should be noted that because these perturbations change the net ecosystem change (relative to the other simulations), the resulting CO_2 concentrations during the spin-up interval will be different than the other simulations. Globally, the 3.6% increase in photosynthetic fluxes caused a 0.10‰ increase in δC_a. Simulated global gross primary production (minus leaf respiration) was 123.9 GtC yr^{-1} for the control simulation, and thus, the ASSIM experiment increased F_A by 4.5 GtC^{-1} yr^{-1}. Given the relationship between F_A and its constituent gross fluxes F_{al} and F_{la}, this change caused the magnitudes of F_{al} and F_{la} to increase by 17 and 12 GtC yr^{-1}, respectively. This implies that the sensitivity of δC_a to increases in assimilation is 0.022‰ (GtC/yr)$^{-1}$ (assuming no change to nonleaf respiration). Despite the increase in mean δC_a, the north-south gradient in δC_a increased by 0.17% (Figure 7e), due primarily to F_{al} fluxes which acted to enrich atmospheric CO_2 in ^{18}O. The enriching effect caused large positive isofluxes to and from leaves in the tropics and reduced negative isofluxes poleward. Indeed, Figure 13a shows how the ASSIM simulation resulted in large changes to δC_a over certain tropical locations and almost no change in some high-latitude regions (e.g., equatorial Africa and Siberia, respectively).

[50] Globally, the RESP experiment increased respiration by 4.4 GtC yr^{-1}. This change to respiration decreased the global mean δC_a by 0.10‰. Thus, the model results suggest that the impact of global respiration on δC_a is 0.023‰ (GtC/yr)$^{-1}$, assuming all other fluxes remain unchanged. In the RESP simulation, the north-south δC_a gradient decreased by 0.061‰ relative to the control simulation (Figure 7e). Similar to the ASSIM simulation, the δC_a change was smallest in the middle and high latitudes (Figure 13b). This pattern was due to the fact that fluxes were much larger in the tropics, and a fractional change to global fluxes has the largest influence on tropical fluxes. The larger increase in isotopically depleted respiration lowered tropical δC_a, which lowered the north-south δC_a gradient.

5. Discussion

5.1. Model and Budget Prediction Comparisons

[51] Some of the perturbation described above can be estimated from budget CO_2 and δC_a equations. If there were no

seasonal variation, the global steady state, $\delta C_{a\text{-ss}}$, can be analyzed following *Cuntz et al.* [2003a] by taking equations (12) and (13) at steady state and solving for the atmospheric isotopic composition:

$$\delta C_{a-\mathrm{ss}} = \frac{F_{\mathrm{la}}\delta C_l + (F_{\mathrm{al}} - F_{\mathrm{la}})\varepsilon_l + F_r \delta F_r + F_{\mathrm{oa}}\delta C_o + (F_{\mathrm{ao}} - F_{\mathrm{oa}})\varepsilon_w + \left(F_f + F_b\right)\delta_{\mathrm{O2}}}{F_{\mathrm{la}} + F_r + F_{\mathrm{oa}} + F_f + F_b} \tag{19}$$

[52] Specifically, the steady state δC_a is a weighted average of the isotopic composition of the contributing fluxes where the weighting is simply the fractional contribution for each flux to gross surface exchange. In this subsection equation (19) is used to compare with the ISOLSM/CAM modeling results for the experiments that changed ecosystem fluxes (F_{la}, F_{al}, and F_r) and those that changed the isotopic composition of precipitation and vapor (and thus δF_{la} and δF_r).

[53] The ASSIM experiment increased leaf fluxes by 3.6% with no change to the isotopic composition of the fluxes (i.e., changes the averaging weights in the budget equation). The budget equation predicts a δC_a increase of 0.10‰, which was also the change in CAM. The results were also similar for the RESP experiment where respiration was increased by 3.6%, both predicting a δC_a decrease of 0.10‰. These results demonstrate the robustness of the budget equation for predicting changes to δC_a for these particular experiments.

[54] When both δW_P and δW_{AV} decrease by 0.32‰ (the PRECWV experiment), modeled δF_{la} and δF_r decrease by 0.32‰ and 0.39‰, respectively. This resulted in a modeled change of −2.6‰. Indeed, when the different values of δF_{la} and δF_r are factored into the budget equation, the predicted change in δC_a is −2.7‰, which is not dissimilar to the results from CAM. When the change is only applied to the tropics, the values of δF_{la} and δF_r change by −1.5‰ and −1.9‰, respectively. In turn, the budget equation predicts a δC_a change of −0.69‰. Interestingly though, ISOLSM/CAM predicts a δC_a change of −1.3‰, almost double the estimate from the budget equation. This discrepancy shows how applying certain changes to one region or one latitudinal zone (as opposed to a global perturbation) can introduce nonlinear effects due to feedbacks within the system. This particular outcome likely resulted from the perturbation only being applied to the tropics and the fact that CO_2 is quickly cycled through the ecosystem within the tropics, a feature that is unresolved with the budget equation.

5.2. Sensitivity of Simulated Seasonal Cycles of δC_a

[55] The sensitivity experiments presented in section 4 not only changed the global mean and spatial variations of δC_a but they also changed the δC_a seasonal cycle. In section 3, it was shown that the model had many shortcomings when predicting the observed seasonal δC_a cycle, though it is possible that one or more of the model experiments could have improved the model/observation comparison. Table 3 shows how the seasonal amplitude compares with the observations for the control simulation and each experiment at four stations (Barrow, Mauna Loa, Cape Grim, and the South Pole). The largest model/observation mismatch in the δC_a seasonal amplitude occurred at the high northern latitude stations (Figure 6a). At Barrow, the simulated seasonal amplitude matched better with observations when the δ^{18}O values of precipitation and/or vapor were decreased in the tropics only (e.g., PRECTWVTROP). This result was largely due to the fact that δC_a is lowered by local ecosystem fluxes during the growing season, and returns to background values when fluxes shut off during winter months. This seasonal effect will have less of an influence if precipitation and vapor δ^{18}O values have a reduced equator-to-pole gradient (as was done in the experiments). To a lesser extent, the amplitude also

Table 3. Model/Observation Difference in the Seasonal Cycle δC_a Amplitude at Barrow (BRW), Mauna Loa (MLO), Cape Grim (CGO), and South Pole (SPO) for the Control and Experimental Simulations[a]

	BRW			MLO			CGO			SPO		
	Surface	Fourth Level	Seventh Level	Surface	Fourth Level	Seventh Level	Surface	Fourth Level	Seventh Level	Surface	Fourth Level	Seventh Level
CTRL	0.671	0.400	−0.084	0.132	0.0768	−0.417	−0.049	−0.021	−0.061	−0.085	−0.097	−0.125
HYD20	0.605	0.356	−0.109	0.134	0.0754	−0.037	−0.045	−0.014	−0.051	−0.078	−0.086	−0.121
HYD300	0.48	0.296	−0.13	0.14	0.0683	−0.034	−0.035	−0.006	−0.044	−0.07	−0.079	−0.121
RH	0.774	0.485	−0.024	0.168	0.105	−0.027	−0.039	−0.013	−0.057	−0.08	−0.093	−0.122
RHTROP	0.646	0.382	−0.099	0.122	0.0617	−0.044	−0.043	−0.015	−0.057	−0.081	−0.093	−0.121
PREC	0.723	0.47	0.0067	0.206	0.108	−0.045	$-3\text{x}10^{-4}$	0.0159	−0.073	−0.069	−0.085	−0.13
WV	0.876	0.542	0.0090	0.185	0.109	−0.024	−0.027	−0.004	−0.062	−0.076	−0.091	−0.123
PREWV	0.929	0.613	0.0999	0.258	0.14	−0.027	0.0227	0.0361	−0.076	−0.06	−0.076	−0.127
PRECTROP	0.341	0.156	−0.268	−0.01	−0.085	−0.093	−0.008	0.0237	−0.055	−0.058	−0.075	−0.109
WVTROP	0.535	0.299	−0.165	0.072	0.0101	−0.06	−0.031	−0.001	−0.057	−0.073	−0.087	−0.116
PRECWVTROP	0.205	0.0547	−0.338	−0.059	−0.128	−0.106	0.0102	0.0435	−0.052	−0.045	−0.063	−0.1
LIGHT	0.727	0.454	−0.049	0.152	0.0933	−0.033	−0.045	−0.016	−0.056	−0.081	−0.092	−0.121
TEMP	0.695	0.423	−0.070	0.143	0.0842	−0.04	−0.046	−0.019	−0.061	−0.085	−0.097	−0.126
ASSIM	0.807	0.533	0.0046	0.168	0.115	−0.008	−0.034	0.0026	−0.041	−0.066	−0.081	−0.11
RESP	0.577	0.309	−0.138	0.111	0.0564	−0.061	−0.058	−0.034	−0.072	−0.098	−0.109	−0.133

[a] Units are ‰.

Table 4. Model/Observation Difference in the Seasonal Cycle δC_a Phase at Barrow (BRW), Mauna Loa (MLO), Cape Grim (CGO), and South Pole (SPO) for the Control and Experimental Simulations[a]

	BRW			MLO			CGO			SPO		
	Surface	Fourth Level	Seventh Level	Surface	Fourth Level	Seventh Level	Surface	Fourth Level	Seventh Level	Surface	Fourth Level	Seventh Level
CTRL	−64.1	−50.9	−31.1	−46.7	−15.9	24	38	42	40.6	52.8	51.5	44.8
HYD20	−63.1	−49.5	−27.6	−46.9	−16.1	22	32.4	37.7	34.4	48.5	46.8	38.4
HYD300	−61.2	−47.2	−24.2	−45.7	−16.7	19.4	28.9	34.5	29.9	45.9	44	34.4
RH	−64.7	−51.6	−31.9	−47.6	−17.3	21	37.5	41.2	38.9	52	50.9	43.8
RHTROP	−64.1	−50.9	−31	−46.3	−15.6	25.5	38.1	41.8	39.7	52.4	51	44.2
PREC	−62.1	−49.3	−32	−46.3	−22.5	13.3	34.2	37.5	36.5	49.1	49.6	45.6
WV	−64.9	−51.8	−32.5	−47.1	−18.2	19.9	37.9	41.3	40.9	53.3	52.9	48.3
PREWV	−63.1	−50.3	−33.2	−46.7	−24.1	10.1	34.5	37.3	36.6	49.6	50.9	51.2
PRECTROP	−64.1	−50.8	−29.5	−39.7	−7.76	49.4	40.3	42.8	44	53.2	52.6	48.9
WVTROP	−64.1	−50.8	−30.4	−44.1	−13	32.6	39.7	43	42.6	53.6	52.7	47.4
PRECWVTROP	−64.1	−50.6	−28.4	−34.5	−1.11	61.5	41.6	43.5	45.9	53.9	53.6	51.5
LIGHT	−64.5	−51.5	−31.8	−47.9	−16.9	23	38	42	40.4	52.9	51.5	44.7
TEMP	−64.5	−51.3	−31.3	−47.1	−16.7	22.8	37	41.1	39.6	52	50.8	44.1
ASSIM	−64.6	−51.5	−31.4	−47.6	−15.7	25.9	36.8	41.2	38.7	52.1	50.6	42.9
RESP	−63.8	−50.6	−30.8	−46.5	−16.3	22.9	38.8	42.6	42.1	53	51.7	45.7

[a]Units are days.

improved for the HYD300 experiment, which caused a global reduction in the isotopic composition of CO$_2$ fluxes from soils (Table 2). This had the largest influence in the tropics, where fluxes are not as seasonal, which caused a reduction in the background δC_a and thus lowered the seasonal amplitude.

[56] Table 4 displays the model/observation mismatch for the δC_a seasonal phase at the same four stations. Unfortunately, the phase of the seasonal cycle did not change significantly for any of the model experiments at Barrow, Cape Grim, or the South Pole. There was a slight change (~ 15 days) at Mauna Loa when the both δW_P and δW_{AV} were decreased in the tropics. The seasonal phase at Mauna Loa is related to the movement of the Hadley Cell, such that it lies under tropical air for most of the year and northern midlatitude air masses during the boreal winter. The reduction in both δW_P and δW_{AV} caused a decrease in the difference between the two air masses and slightly shifts the timing of the drop in δC_a. However, Mauna Loa was not a location where the phase of the δC_a seasonal cycle was particularly problematic. Furthermore, these results suggest that the seasonal phase model shortcomings at middle and high latitudes are likely related to the seasonal timing of one or more δC_a driving variable, rather than mean global or tropical model biases.

5.3. Additive Influence of Variables

[57] Additional experiments were performed that examined how certain variables that are related to one another affect the simulated δC_a. The purpose of the additional simulations is to examine the degree to which the response of modeled δC_a to multiple variable changes is additive. These simulations were done with respect to the simulation that increased global atmospheric temperatures by 1 K, the TEMP experiment. Assuming that vapor and precipitation δ^{18}O values also increase according to the approximate slope of 0.7‰ K^{-1} [*Johnsen et al.*, 1989], two experiments were conducted that applied a 0.7‰ increase to the water isotopologues, both with and without the 1 K increase. Another set of experiments decreased relative humidity by 4% (which is approximately the relative humidity change at 20°C and a relative humidity of 70%), both with and without the temperature change.

[58] When both δW_P and δW_{AV} increase globally, δC_a responds by increasing by 0.612‰, which is consistent with the results of the PRECWV simulation, but scaled down. When this isotopic forcing perturbation is applied with the 1 K increase in temperature, the model predicts a global δC_a change of 0.48‰. Though dependent on the choice of the temperature-isotope slope (which others have predicted to be lower), these model results would suggest that the influence on δC_a from the 1 K increase in air temperatures would get outweighed by the subsequent increase in precipitation and vapor δ^{18}O values. Furthermore, the results from section 4.4 showed how δC_a decreased globally by 0.13‰ with only a 1 K increase in global atmospheric temperatures. Thus, the additional simulations indicate that the response of δC_a to both the temperature and isotope hydrology perturbations is similar and almost identical to the additive response to each perturbation.

[59] Another additional experiment decreased relative humidity by 4% (4 percentage points), while increasing air temperature by 1 K. The global change in δC_a from this experiment was an increase of 0.13‰. When only the decrease in relative humidity was applied to the forcing, the global mean value of δC_a increased by 0.27‰. Again, because increasing temperatures by 1 K alone caused δC_a to decrease by 0.13‰ implies that the two influences are nearly linear. However, unlike the previous scenario, the temperature influence was slightly stronger (though only by 0.01‰) when combined with the relative humidity change.

6. Conclusion

[60] A mechanistic, isotope-enabled land model (ISOLSM) was used to simulate global terrestrial fluxes of CO$_2$, including their oxygen isotope composition. These were then combined with additional CO$_2$ fluxes such as ocean gas exchange and fossil fuel emissions in a three-dimensional global transport model (CAM) to simulate atmospheric CO$_2$ and CO^{18}O. This framework accurately captured the global mean, north-south gradient, and to a lesser extent, the seasonal cycle of δC_a. To develop an understanding of the controls on observed annual mean and spatial variations in δC_a, model sensitivity

experiments were performed to examine the effects of changes in soil CO$_2$ hydration rates, relative humidity, δ^{18}O values of precipitation and water vapor (δW_P and δW_{AV}), radiation levels, temperature, and assimilation/respiration partitioning on δC_a. The sizes of each of the perturbations were based on observed variations discussed elsewhere [e.g., *Robock*, 2000; *Gu et al.*, 2003; *Buenning et al.*, 2011].

[61] The results presented here suggest that δC_a is strongly dependent on hydrologic changes, such as changes to relative humidity and isotope hydrology (i.e., δW_P and δW_{AV}), an indication that the global mean δC_a responds principally to changes in the isotopic composition of leaf and soil water rather than global changes to ecosystem CO$_2$ fluxes. Our results are consistent with recent studies that have suggested that water isotope forcing and relative humidity had the largest influence on the observed interannual δC_a variations [*Buenning et al.*, 2011; *Welp et al.*, 2011].

[62] The other main objective of this study was to characterize controls on the spatial variations of δC_a, and in particular the north-south δC_a gradient. *Wingate et al.* [2009] showed that the simulated gradients were increased and better matched with observations when soil CO$_2$ hydration rates were increased by factors of 20 and 300. Similar to their results, the model used in this study showed an increase in the gradient (of comparable magnitude) when hydration rates were increased by the same factors. However, it did not improve the global and zonal mean data model comparison; in fact, it made the comparisons worse. Our model experiments suggested that the gradient could also be increased by decreases in global or middle- and high-latitude values of δW_p and δW_{AV} (which also decreased global mean δC_a). To a lesser extent, increased global and middle- and high-latitude relative humidity also caused nontrivial increases to the north-south δC_a gradient. Variations to the CO$_2$ flux partitioning also caused the north-south δC_a gradient to change, such that the gradient increased when leaf fluxes increased (and nonleaf respiration remained unchanged relative to the control) and decreased when nonleaf respiration increased (but photosynthesis was not changed).

[63] The isotope hydrology experiments are particularly interesting in the context of the simulations of *Wingate et al.* [2009], in that many isotope-equipped global models fail to simulate the proper depletion in δW_p at middle and high latitudes. *Noone and Sturm* [2010] showed that, over northern Canada and Siberia, GCMs commonly simulated precipitation δ^{18}O values that were not low enough. Furthermore, the results shown here suggest that the gradient is most sensitive to δW_p and δW_{AV}, especially in the middle and high latitudes. So it is not surprising that a modeled north-south gradient would be too low if both δW_p and δW_{AV} were too high outside of the tropics and subtropics, which might have been the case for the control simulation of *Wingate et al.* [2009] (which simulated a too-weak north-south gradient). Recall that the values of δW_p and δW_{AV} used here were constrained by GNIP observations, so such a bias did not occur for the model used in this study, and in turn, the CTRL simulation accurately captured the north-south δC_a gradient. This study does not contradict findings elsewhere for a strong potential influence of soil CO$_2$ hydration rates on the north-south δC_a gradient, but rather our control simulation already captured the gradient accurately, likely due to correct water isotope gradients. In fact, the model results presented here suggest that even modest changes to the global mean or spatial variations of δW_p and δW_{AV} can strongly influence the north-south δC_a gradient.

Appendix A: Notation

C_a	CO$_2$ mixing ratio in the atmosphere, mole fraction.
$^{18}C_a$	CO^{18}O mixing ratio in the atmosphere, mole fraction.
C_C	CO$_2$ mixing ratio at the surface chloroplast within leaf stomata, mole fraction.
C_i	CO$_2$ mixing ratio inside the stomatal pores, mole fraction.
F_{al}	CO$_2$ flux into leaves, mol m^{-2} s^{-1}.
$^{18}F_{\mathrm{al}}$	CO^{18}O flux into leaves, mol m^{-2} s^{-1}.
F_{ao}	CO$_2$ flux into the ocean surface, mol m^{-2} s^{-1}.
$^{18}F_{\mathrm{ao}}$	CO^{18}O flux into the ocean surface, mol m^{-2} s^{-1}.
F_b	CO$_2$ flux from biomass burning, mol m^{-2} s^{-1}.
$^{18}F_b$	CO^{18}O flux from biomass burning, mol m^{-2} s^{-1}.
F_{la}	CO$_2$ flux out of leaves, mol m^{-2} s^{-1}.
$^{18}F_{\mathrm{la}}$	CO^{18}O flux out of leaves, mol m^{-2} s^{-1}.
F_f	CO$_2$ flux due to fossil fuel consumption, mol m^{-2} s^{-1}.
$^{18}F_f$	CO^{18}O flux due to fossil fuel consumption, mol m^{-2} s^{-1}.
F_A	Gross Primary Product minus leaf respiration, mol m^{-2} s^{-1}.
F_o	Net flux of CO$_2$ from ocean water, mol m^{-2} s^{-1}.
F_{oa}	CO$_2$ flux from the ocean surface, mol m^{-2} s^{-1}.
$^{18}F_{\mathrm{oa}}$	CO^{18}O flux from the ocean surface, mol m^{-2} s^{-1}.
F_r	CO$_2$ flux from soil respiration, mol m^{-2} s^{-1}.
$^{18}F_r$	CO^{18}O flux from soil respiration, mol m^{-2} s^{-1}.
h_l	Relative humidity at leaf surface, range of 0 to 1.0.
I_{la}	Isoflux from leaf-to-atmosphere fluxes, ‰ mol m^{-2} s^{-1}.
I_r	Isoflux from soil respiration, ‰ mol m^{-2} s^{-1}.
K_{ex}	Air-sea gas exchange coefficient, mol m^{-2} s^{-1} Pa^{-1}.
M_a	Unit conversion factor, moles of air m^{-2}.
p_a	Partial pressure of CO$_2$ in the atmosphere, Pa.
p_o	Partial pressure of CO$_2$ at ocean surface, Pa.
PSN	Photosynthesis, mol m^{-2} s^{-1}.
Q_E	Soil evaporation, μmol m^{-2} s^{-1}.
Q_V	Transpiration from vegetatoin, μmol m^{-2} s^{-1}.
R_{lw}	^{18}O isotopic ratio of leaf water.
R_l	^{18}O isotopic ratio of CO$_2$ equilibrated with leaf water.
R_o	^{18}O isotopic ratio of CO$_2$ equilibrated with surface ocean water.
R_{ow}	^{18}O isotopic ratio of surface ocean water.
R_{O2}	^{18}O isotopic ratio of atmospheric O$_2$.
R_{sw}	^{18}O isotopic ratio of root-weighted soil water.
R_s	^{18}O isotopic ratio of CO$_2$ equilibrated with root-weighted soil water.
R_{cv}	^{18}O isotopic ratio of canopy water vapor.
R_v	^{18}O isotopic ratio of atmospheric water vapor.
R_{VPDB}, R_{VSMOW}	2.08835×10^{-3}, 2.0052×10^{-3}.
T_s	Surface temperature of either: ocean, soil, or vegetation, K.
α_{eq}	Temperature-dependent CO$_2$ equilibration factor.
α_l	Effective kinetic fractionation factor for CO^{18}O diffusion in and out of the stomata.
α_w	Effective kinetic fractionation factor for CO^{18}O diffusion in and out of surface ocean water.
δC_a	δ^{18}O-CO$_2$ value of free air, ‰ versus VPDB-CO$_2$.
δC_l	δ^{18}O-CO$_2$ value of CO$_2$ equilibrated with leaf water, ‰ versus VPDB-CO$_2$.
δC_o	δ^{18}O-CO$_2$ value of CO$_2$ equilibrated with surface ocean water, ‰ versus VPDB-CO$_2$.
δC_S	δ^{18}O-CO$_2$ value of CO$_2$ equilibrated with soil water, ‰ versus VPDB-CO$_2$.
δF_{la}	δ^{18}O-CO$_2$ value of leaf-to-atmosphere CO$_2$ flux, ‰ versus VPDB-CO$_2$.
δF_r	δ^{18}O-CO$_2$ value of soil respiration, ‰ versus VPDB-CO$_2$.
δW_{AV}	δ^{18}O value of atmospheric water vapor, ‰ versus VSMOW-H$_2$O.
δW_{CV}	δ^{18}O value of canopy water vapor, ‰ versus VSMOW-H$_2$O.
δW_l	δ^{18}O value of leaf water, ‰ versus VSMOW-H$_2$O.
$\delta W_{l\text{-CG}}$	δ^{18}O value of leaf water using the Craig-Gordon estimation, ‰ versus VSMOW-H$_2$O.
δW_P	δ^{18}O value of precipitation, ‰ versus VSMOW-H$_2$O.

δW_S	$\delta^{18}O$ value of root-weighted soil water, ‰ versus VSMOW-H_2O.
ε_l	Effective kinetic fractionation factor for $CO^{18}O$ diffusion in and out of the stomata, ‰.
ε_w	Effective kinetic fractionation factor for $CO^{18}O$ diffusion in and out of surface ocean water, equal to +0.8‰.
ε_{eq}	Temperature-dependent CO_2 equilibration factor in δ notation.
ε_k	$H_2{}^{18}O$ kinetic fractionation factor for molecular diffusion.
ε_{LV}	The temperature-dependent equilibrium fractionation of $H_2{}^{18}O$ during the liquid-vapor phase transition.

Appendix B: Determining Potential Drivers of δC_a

[64] Five fluxes are principally responsible for CO_2 variations in the atmosphere, and these processes also dominate the global δC_a budget [*Farquhar et al.*, 1993; *Ciais et al.*, 1997a, 1997b]: photosynthetic assimilation, soil respiration, ocean exchanges, fossil fuel emissions, and biomass burning. Considering just these exchanges, the global budget for δC_a can be written as

$$\frac{d\delta C_a}{dt} = \frac{1}{C_a M_a}\left[F_A\Delta_A + F_r\Delta_r + F_o\Delta_o + \left(F_f + F_b\Delta_f\right)\right] \quad \text{(B1)}$$

where C_a is atmospheric CO_2 mixing ratio, M_a is a flux conversion factor (mol air m^{-2}), F stands for CO_2 fluxes (mol m^{-2} s^{-1}), Δ refers to (apparent) discriminations against $CO^{18}O$ (in ‰). Subscripts A, r, o, f, and b refer to assimilation, respiration, ocean, fossil fuel, and biomass burning, respectively. The first two terms within the brackets of equation (B1) can be written as [*Farquhar et al.*, 1993; *Ciais et al.*, 1997a]

$$F_A\Delta_A = F_A\left[\frac{C_C}{C_a - C_C}(\delta C_1 - \delta C_a) - \varepsilon_l\right] \quad \text{(B2)}$$

$$F_r\Delta_r = F_r[(\delta C_S - \delta C_a) + \varepsilon_S] \quad \text{(B3)}$$

where C_C is the CO_2 mixing ratio at the surface of the chloroplast within leaf stomata, ε values are kinetic fractionation factors associated with diffusion, and subscripts l and S refer to leaves and soil, respectively. It can be seen from equations (B1) to (B3) that δC_a can be affected by changes in the magnitude of terrestrial CO_2 fluxes and in the isotopic composition of leaf and soil CO_2.

[65] Assimilation and stomatal conductance are principally sensitive to the photosynthetic photon flux density, relative humidity, air temperature, and CO_2 concentrations [*Jarvis*, 1976; *Wong et al.*, 1978; *Stewart*, 1988; *Jones and Higgs*, 1989; *Collatz et al.*, 1991]. The photosynthesis-temperature relationship is particularly complicated because it involves both direct and indirect effects (through changes in relative humidity) that oppose one another. Nonetheless, these three variables (photon flux density, humidity, and temperature) can directly alter leaf CO_2 fluxes and thereby cause changes in δC_a.

[66] Root growth and maintenance respiration and heterotrophic respiration produces CO_2 in the soil that takes on the isotopic signature of local water (i.e., either root or bacterial medium soil water) via the dissolution and hydration of CO_2 molecules within soil water. The isotopic composition of soil-respired CO_2 is modified by differences in diffusion rates of CO_2 and $CO^{18}O$ through the soil column, and concurrent isotopic equilibration with soil water [*Hesterberg and Siegenthaler*, 1991]. Another process that influences δC_a is the "invasion effect" in which atmospheric CO_2 diffuses into the top layer of the soil, attains the isotopic signature of the surface soil water through rapid isotopic equilibration, and diffuses back to the atmosphere [*Tans*, 1998; *Riley*, 2005]. This invasion process is influenced by soil temperature, soil water content, the hydration rate, and atmospheric mixing conditions adjacent to the surface, which in turn are influenced by radiation, evaporation, and the concentration of CO_2 immediately above the soil surface [*Tans*, 1998; *Miller et al.*, 1999; *Stern et al.*, 2001; *Riley*, 2005; *Henderson-Sellers et al.*, 2006; *McDowell et al.*, 2008; *Wingate et al.*, 2009].

[67] The ^{18}O compositions of leaf and soil CO_2 are controlled by the isotopic composition of leaf and soil water pools, respectively. In leaves, the ^{18}O exchange occurs primarily in the water of the mesophyll cells (adjacent to the stomatal cavity) [*Farquhar and Lloyd*, 1993; *Gillon and Yakir*, 2000]. In the presence of the ubiquitous enzyme carbonic anhydrase, the catalyzed reaction occurs almost instantaneously [*Gillon and Yakir*, 2001]. During transpiration, the lighter water isotopologue evaporates and diffuses through the stomata more efficiently than the heavy isotopologue, thereby enriching leaf water in the heavy isotopes of hydrogen and oxygen. *Craig and Gordon* [1965] formulated a model to predict the isotopic composition of evaporating surface waters, which can be modified for leaves [*Flanagan et al.*, 1991] to show that during steady state conditions, the isotopic composition ($\delta W_{l\text{-CG}}$) at the evaporation site can be written as

$$\delta W_{l-CG} = \varepsilon_{LV} + (1 - h_l)(\delta W_X - \varepsilon_k) + h_l \delta W_{CV} \quad \text{(B4)}$$

where ε_{LV} is the temperature-dependent equilibrium fractionation of $H_2{}^{18}O$ during the liquid-vapor phase transition [*Majoube*, 1971], ε_k is the kinetic fractionation of $H_2{}^{18}O$ during the diffusion of vapor across the stomata and leaf boundary layer [*Cappa et al.*, 2003; *Luz et al.*, 2009], h_l is relative humidity above the evaporating surface, δW_X is the isotopic composition of xylem water, and δW_{CV} is the isotopic composition of canopy vapor (a complete list of the variable notation is provided in Appendix A). This simple mass balance equation shows that the isotopic composition of leaf water (δW_l) is related to that of stem/xylem water (δW_X) and canopy vapor (δW_{CV}), the relative humidity at the leaf surface (h_l), and leaf temperature (through equilibrium fractionation). Other factors can influence δW_l, including the Péclet effect [*Farquhar and Lloyd*, 1993] and leaf water content. In the extreme case of a relative humidity equal to zero causes the leaf water isotopic ratio to depend only on δW_X (i.e., transpiration is assumed to be a one-way flux out of the leaf). Likewise, a relative humidity of 100% creates a thermodynamic equilibrium between water in the leaf and the ambient vapor and the kinetic isotope effect is eliminated, with δW_l dependent only on δW_{CV} and ε_{LV}. Therefore, changes in humidity can have significant impacts on the isotopic composition of leaf water, and consequently δC_l and potentially δC_a.

[68] Xylem water is derived from soil water, and δW_X reflects a convolution of vertical variations in root water uptake and the $^{18}O/^{16}O$ composition of soil water (δW_S) in the absence of stem capacitance with a differing isotope composition. δW_S depends primarily on the isotopic composition of precipitation (δW_P) and soil evaporation. As such, any variation in δW_P could potentially cause changes in the isotopic

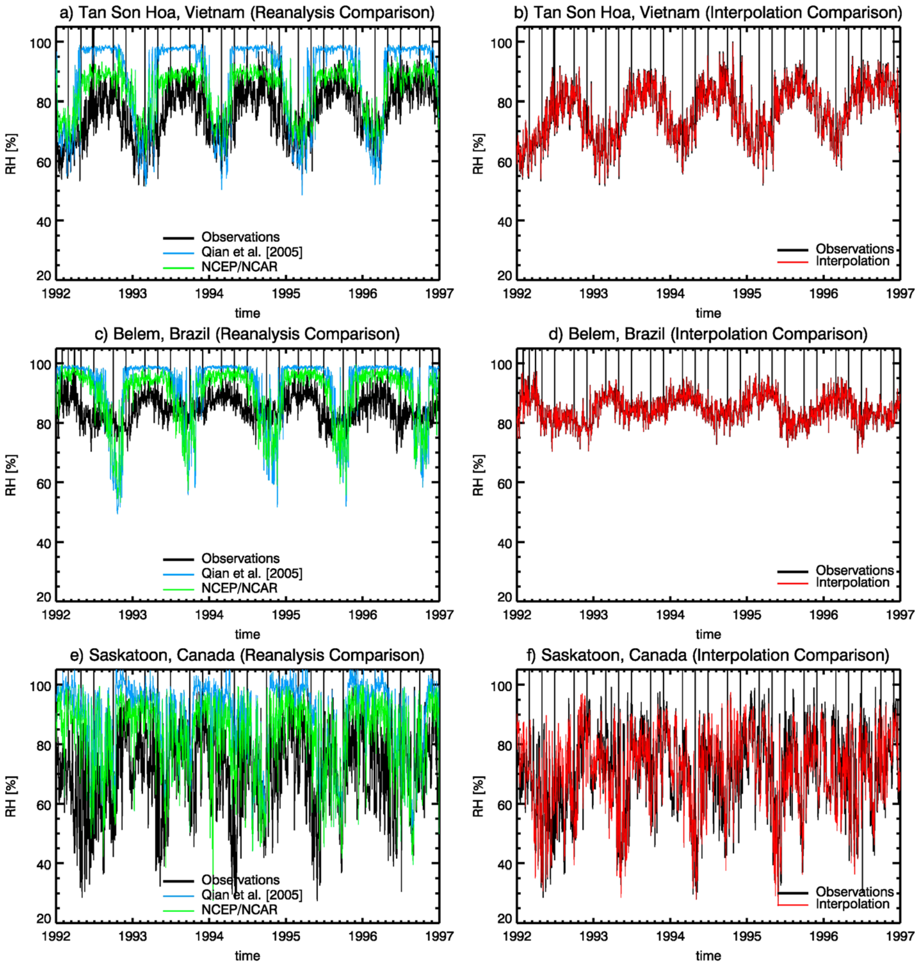

Figure C1. Comparison between observed variations in relative humidity and relative humidity from gridded data sets at (a and b) Tan Son Hoa, Vietnam, (c and d) Belem, Brazil, and (e and f) Saskatoon, Canada. The black line shows the station observations, the blue line shows the reanalysis data from *Qian et al.* [2006], green line represents the NCEP Reanalysis, and the red line is the interpolated data used to force ISOLSM.

composition of soil, stem, and leaf water (via equation (B4)). Similarly, the isotopic composition of canopy vapor is primarily controlled by the isotopic composition of above-canopy atmospheric vapor (δW_{AV}), although *Still et al.* [2009] showed how canopy transpiration in low-stature and high aerodynamic resistance canopies can provide a feedback on the isotopic composition of in-canopy vapor. These relationships indicate that δC_S, δC_l, and subsequently δC_a could be sensitive to changes in the isotopic composition of precipitation and atmospheric vapor (i.e., changes in isotope hydrology). Thus, δC_a could be influenced by many carbon and water cycle variables, and the focus of this study is to quantify how the global mean and spatial structure of δC_a responds to changes in these variables.

Appendix C: World Meteorological Organization Forcing Data

[69] A Cressman-like objective analysis [*Cressman*, 1959] is used to interpolate World Meteorological Organization (WMO) station observations onto a grid. The procedure entails finding the weighted mean value of some quantity X (e.g., relative humidity or temperature) on a grid, given a number of values X_j with irregularly distributed positions λ_j, ϕ_j. That is,

$$X(\lambda, \phi) = \frac{1}{A(\lambda, \phi)} \frac{\sum_j X_j W(d_j) \cos\phi_j}{\sum_j W(d_j) \cos\phi_j} \tag{C.1}$$

where A is the area of each grid cell, and included for quantities needed in per unit area. An example is where a probability distribution of observational points is desired and where X is set to one for all points j, and the resulting field has units of probability per unit area. The weight W is a function of the great circle distance (d_j) between each grid cell center and each observation,

$$W(d_j) = \frac{R_c^2 - d_j^2}{R_c^2 + (\gamma^{-1} - 1) d_j^2} \tag{C.2}$$

where R_c is a critical radius that ensures W is positive for all d_j larger than the critical radius, R_c. The shape of the weighting

Table D1. Model-Observation Differences in CO_2 Seasonal Cycles

				Amplitude Difference[a]			Phase Difference[a]		
	Longitude (°E)	Latitude (°N)	Height (m)	Surface (ppm)	Fourth Level (ppm)	Seventh Level (ppm)	Surface (days)	Fourth Level (days)	Seventh Level (days)
Alert	−62.51	82.45	200	8.02	5.49	−0.413	−8.62	−6.45	0.337
Ny-Alesund	11.89	78.91	474	7.05	4.57	−0.959	−3.17	−1.60	5.85
Summit	−38.42	72.60	3209	9.30	5.33	−0.398	−5.75	−2.01	5.47
Barrow	−156.61	71.32	11	10.8	4.45	−1.76	−10.9	−2.43	7.36
Ocean Station M	2.00	66.00	0	5.73	4.46	−1.00	−6.20	−2.46	5.92
Storhofdi	−20.29	63.40	118	5.48	4.08	−1.21	−2.25	0.492	7.46
Baltic Sea	17.22	55.35	3	6.43	2.15	−5.58	17.2	23.0	37.0
Cold Bay	−162.72	55.21	21	0.718	−0.106	−3.83	11.5	15.0	17.8
Mace Head	−9.90	53.33	5	3.42	2.40	−2.47	2.07	3.60	12.0
Shemya Island	−174.13	52.71	23	0.693	−0.470	−5.21	10.6	12.1	15.2
Hegyhatsal	16.65	46.96	248	−10.1	−8.16	−16.6	46.4	42.6	65.0
Ulaan Uul	111.10	44.45	1007	1.23	−1.02	−5.08	10.9	11.9	26.0
ST, Kazakastaan	76.87	44.08	595	−2.70	−1.68	−5.93	26.5	32.3	49.2
PA, Kazakastaan	77.88	43.25	2519	−2.21	−2.45	−4.68	21.8	28.6	42.4
Niwot Ridge	−105.59	40.05	3523	−2.57	−1.61	−0.177	19.2	10.1	24.9
Wendover	−113.72	39.90	1327	8.18	2.83	−0.552	0.429	3.06	20.9
Point Arena	−123.74	38.95	17	−8.34	−2.09	−2.50	12.9	30.8	39.7
Tae-ahn	126.13	36.74	16	−1.39	−1.88	−4.76	8.24	1.76	19.7
Mt. Waliguan	100.90	36.29	3810	1.84	1.09	−0.549	4.56	3.43	13.3
Tudor Hill	−64.88	32.26	30	3.14	3.11	−0.798	−11.1	−11.6	13.5
Negev	34.78	30.86	477	0.519	0.475	−1.24	26.5	28.8	42.9
Pacific 30N	−135	30.00	10	0.820	0.753	−1.65	5.65	13.4	21.6
Tenerife	−16.50	28.31	2372	0.648	1.68	0.763	10.6	1.77	10.1
Key Biscayne	−80.16	25.67	1	1.68	1.74	0.616	−15.9	−5.29	13.0
Asskrem	5.42	23.18	1842	3.32	2.79	0.648	−15.8	−12.0	7.36
Mauna Loa	−155.58	19.54	3397	3.28	3.48	1.56	−17.7	−16.3	−11.3
Cape Kumukahi	−154.82	19.52	3	1.49	1.69	−0.233	−3.83	−2.49	2.55
Pacific 15N	−145.00	15.00	10	0.696	1.35	−0.250	−11.8	−9.60	−4.32
Ragged Point	−59.43	13.16	15	1.42	1.39	0.499	4.80	5.13	2.48
Christmas Island	−157.15	1.7	0	1.34	0.823	1.20	2.60	−1.49	16.1
Mahe Island	55.53	−4.68	2	−1.86	−1.52	−1.48	330	124	175
Ascension Island	−14.40	−7.97	85	3.48	4.42	2.14	−22.5	8.64	−47.6
Pacific 10S	−161.00	−10.00	10	0.429	0.923	1.14	152	144	130
Tutuila	−170.56	−14.25	42	1.31	1.72	1.84	−134	−158	−159
Pacific 20S	−174.00	20.00	10	1.54	1.54	2.20	−46.9	−58.2	−110
Pacific 25S	−171.00	−25.00	10	2.20	2.43	2.74	−64.3	−63.6	−95.2
Easter Island	−109.43	−27.16	47	1.73	1.89	2.35	−62.9	−64.6	−83.8
Pacific 30S	−176.00	−30.00	10	2.40	2.64	3.44	−31.2	−34.9	−56.8
Cape Grim	144.69	−40.68	94	1.51	1.70	2.89	−7.12	0.945	1.61
Crozet Island	51.85	−46.43	197	1.24	1.31	1.78	5.20	12.7	15.0
Tierra del Fuego	−68.31	−54.85	12	2.05	0.976	1.26	−7.54	46.1	54.1
Palmer	−64.00	−64.92	10	1.09	1.16	1.24	13.2	17.9	21.6
Syowa	39.58	−69.00	0	1.65	1.67	1.87	19.8	18.2	17.8
Halley	−26.21	−75.61	30	1.53	1.56	1.68	24.6	22.2	19.6
South Pole	−24.80	−89.98	2810	1.51	1.56	1.59	16.8	13.4	15.1

[a] Model minus observed.

is modified by the "pinching" factor (γ), such that the mean radius of the weighting is reduced with smaller values.

[70] This method results in missing values when the critical radius is small enough. On the other hand, the spatial structure of a variable may be compromised due to over smoothing when the critical radius is too big. To avoid these problems, the objective analysis is looped 6 times for each day, such that the critical radius goes from large to small (R_c = 5000, 1000, 800, 600, 400, and 200 km), and the pinching factor starts extremely small and only gets larger for the first two loops (γ = 0.0002, 0.002, 0.02, 0.02, 0.02, and 0.02). Thus, the previous value with the larger radius is used to fill in grid cells with missing values. This approach ensures that local-scale features are retained where data coverage is good, but provides an interpolated value where observations are sparse.

[71] The chosen grid has a horizontal resolution given by triangular truncation of the spherical harmonic spectrum at wave number 62, which corresponds to a Gaussian grid of about 1.875° longitude × 1.875° latitude. The computational grid is the same as the reanalysis data set of *Qian et al.* [2006], which has eight time samples per day. For each day and for each grid cell in the *Qian et al.* [2006] data set, daily means were calculated and removed for each of the eight time samples. The remaining "anomalies" are then added to the interpolated WMO data, thus imposing a diurnal cycle onto the observed daily means.

[72] To demonstrate that this method accurately captures the station observations, Figure C1 compares examples of the observed seasonal cycle with the nearest neighbor grid cell for the interpolated data set, the data set of *Qian et al.* [2006], and the National Centers for Environmental Prediction (NCEP) reanalysis [*Kalnay et al.*, 1996]. The comparison is done for three stations in three separate regions (two tropical and one midlatitude). The station

Table D2. Model-Observation Differences in δC_a Seasonal Cycles

				Amplitude Difference[a]			Phase Difference[a]		
	Longitude (°E)	Latitude (°N)	Height (m)	Surface (ppm)	Fourth Level (ppm)	Seventh Level (ppm)	Surface (days)	Fourth Level (days)	Seventh Level (days)
Alert	−62.51	82.45	200	0.532	0.369	−0.111	−34.6	−32.8	−15.4
Ny-Alesund	11.89	78.91	474	0.616	0.534	0.103	−49.6	−47.8	−33.2
Summit	−38.42	72.60	3209	0.579	0.393	−0.0825	−56.4	−50.5	−37.5
Barrow	−156.61	71.32	11	0.671	0.400	−0.0841	−64.1	−50.9	−31.1
Ocean Station M	2.00	66.00	0	0.463	0.389	0.0232	−46.6	−47.0	−34.7
Storhofdi	−20.29	63.40	118	0.506	0.433	0.0208	−46.0	−45.4	−30.8
Baltic Sea	17.22	55.35	3	−0.402	−0.546	−0.844	−27.5	−44.5	−36.2
Cold Bay	−162.72	55.21	21	0.0517	0.0157	−0.431	−27.6	−29.4	−14.6
Mace Head	−9.90	53.33	5	0.192	0.0946	−0.351	−44.4	−42.2	−24.5
Shemya Island	−174.13	52.71	23	0.114	0.0665	−0.498	−38.1	−40.1	−23.6
Hegyhatsal	16.65	46.96	248	−1.30	−1.44	−1.76	−58.0	−52.9	−44.1
Ulaan Uul	111.10	44.45	1007	−0.186	−0.287	−0.530	−72.4	−61.4	−42.8
ST, Kazakastaan	76.87	44.08	595	−1.16	−1.23	−1.67	−79.8	−79.9	−56.8
PA, Kazakastaan	77.88	43.25	2519	−0.450	−0.488	−0.820	−74.2	−77.3	−56.8
Niwot Ridge	−105.59	40.05	3523	−0.327	−0.387	−0.478	−64.9	−47.2	−45.1
Wendover	−113.72	39.90	1327	−0.00869	−0.280	−0.592	−84.9	−47.9	−51.4
Point Arena	−123.74	38.95	17	0.569	0.0611	−0.174	−43.0	−15.4	−4.96
Tae-ahn	126.13	36.74	16	0.0903	−0.203	−0.559	−21.5	11.6	17.6
Mt. Waliguan	100.90	36.29	3810	−0.187	−0.284	−0.484	−90.5	−71.8	−51.3
Tudor Hill	−64.88	32.26	30	−0.179	−0.216	−0.478	−36.7	−33.3	−40.1
Negev	34.78	30.86	477	−0.404	−0.454	−0.633	−5.49	6.13	−6.05
Pacific 30N	−135	30.00	10	0.199	−0.0516	−0.344	−47.1	−22.3	7.38
Tenerife	−16.50	28.31	2372	0.143	0.0271	−0.203	−57.8	−42.7	−36.5
Key Biscayne	−80.16	25.67	1	−0.0463	−0.0934	−0.277	−2.96	−4.34	−9.58
Asskrem	5.42	23.18	1842	0.185	0.193	−0.0536	−52.8	−62.7	−70.0
Mauna Loa	−155.58	19.54	3397	0.132	0.0768	−0.0417	−46.7	−15.9	24.0
Cape Kumukahi	−154.82	19.52	3	−0.0371	−0.0924	−0.211	−50.3	−19.5	20.5
Pacific 15N	−145.00	15.00	10	−0.0951	−0.0789	−0.160	−59.6	−25.6	11.9
Ragged Point	−59.43	13.16	15	−0.00464	−0.113	−0.123	−72.4	−69.0	−45.4
Christmas Island	−157.15	1.7	0	−0.0400	−0.0329	−0.218	−10.2	−9.89	−7.11
Mahe Island	55.53	−4.68	2	−0.143	−0.139	−0.142	−7.70	5.91	−10.4
Ascension Island	−14.40	−7.97	85	−0.0623	−0.0301	0.0660	52.3	92.2	2.20
Pacific 10S	−161.00	−10.00	10	0.0452	0.0738	−0.0663	14.1	15.1	30.5
Tutuila	−170.56	−14.25	42	−0.0403	0.00273	−0.0951	17.3	32.3	46.8
Pacific 20S	−174.00	20.00	10	−0.137	−0.123	−0.130	−51.1	−34.4	39.1
Pacific 25S	−171.00	−25.00	10	−0.106	−0.102	−0.102	−124.1	−104.5	55.3
Easter Island	−109.43	−27.16	47	−0.165	−0.159	−0.168	61.3	56.2	22.2
Pacific 30S	−176.00	−30.00	10	−0.130	−0.129	−0.0567	57.0	58.4	37.0
Cape Grim	144.69	−40.68	94	−0.0488	−0.0211	−0.0605	38.0	42.0	40.6
Crozet Island	51.85	−46.43	197	−0.151	−0.157	−0.188	53.9	59.2	52.4
Tierra del Fuego	−68.31	−54.85	12	0.0267	−0.140	−0.149	17.4	33.4	28.9
Palmer	−64.00	−64.92	10	−0.0689	−0.0575	−0.0798	47.8	46.1	38.2
Syowa	39.58	−69.00	0	−0.0707	−0.0718	−0.0893	53.0	52.5	53.8
Halley	−26.21	−75.61	30	−0.0195	−0.0180	−0.0236	55.9	53.1	47.8
South Pole	−24.80	−89.98	2810	−0.0852	−0.0971	−0.125	52.8	51.5	55.8

[a] Model minus observed.

chosen for the comparison were ones with long observational records that show clear interannual variability and seasonal cycles. For both tropical regions, the two reanalysis data sets overpredict the amplitude of the seasonal cycle, with wet-season values that are too high and close to 100%. The interpolated data set accurately matches the station observation. In the midlatitudes, the seasonal cycle in relative humidity is not as clear with no monsoon to bring in a dry and wet season. Instead, the variations are dominated by atmospheric waves that bring in moisture every 5 to 7 days on average. This particular midlatitude region does observe an annually occurring dry period during the late spring/early summer. In the reanalysis data, the dry period is slightly later in the year, and thus, the seasonal cycle is not accurately captured. The interpolated data again matches up well with the stations observations, and the timing of the dry period is correct. These comparisons are the reason why the interpolated data set is preferred over the reanalysis data to force ISOLSM. Given the importance of relative humidity found here, it is particularly important to force the model with realistic relative humidity.

Appendix D: Seasonality Statistics

[73] Tables D1 and D2 contain the amplitude and phase differences between the observations and the model for CO_2 and δC_a, respectively. These differences were calculated from the curves shown in Figures 4 and 5.

[74] **Acknowledgments.** We acknowledge with appreciation support from the NOAA Climate Program Office (award NA03OAR4310059). This research was also supported by the Director, Office of Science, Office of Biological and Environmental Research, Climate and Environmental Science Division, of the U.S. Department of Energy under contract DEAC02-05CH11231 to Berkeley Lab. We thank the associate Editor and two anonymous reviewers for their extensive and valuable comments and suggestions.

References

Andres, R. J., G. Merland, I. Fung, and E. Matthews (1996), A 1 × 1 distribution of carbon dioxide emissions from fossil fuel consumption and cement manufacture, 1950–1990, *Global Biogeochem. Cycles*, *10*, 419–429.

Aranibar, J. N., Berry, J. A., Riley, W. J., Pataki, D. E., Law, B. E., and Ehleringer, J. R. (2006), Combining meteorology, eddy fluxes, isotope measurements, and modeling to understand environmental controls of carbon isotope discrimination at the canopy scale, *Global Change Biol.*, *12*, 710–730, doi:10.1111/j.1365-2486.2006.01121.x.

Ballantyne, A. P., C. B. Alden, J. B. Miller, P. P. Tans, and J. W. C. White (2012), Increase in observed net carbon dioxide uptake by land oceans during the past 50 years, *Nature*, *48*, 7409, doi:10.1038/nature11299.

Bonan, G. (1996), A land surface model (LSM version 1.0) for ecological, hydrological, and atmospheric studies: Technical description and user's guide, TN-417+STR, Natl. Cent. For Atmos. Res., Boulder, Colo.

Brenninkmeijer, C., K. Kraft, and W. Mook (1983), Oxygen isotope fractionation between CO_2 and H_2O, *Isot. Geosci.*, *1*, 181–190.

Buenning, N. H., D. C. Noone, W. J. Riley, C. J. Still, and J. W. C. White (2011), Influences of the hydrological cycle on observed interannual variations in atmospheric CO^{18}O, *J. Geophys. Res.*, *116*, G04001, doi:10.1029/2010JG001576.

Cappa, C. D., M. B. Hendricks, D. J. DePaolo, and R. C. Cohen (2003), Isotopic fractionation of water during evaporation, *J. Geophys. Res.*, *108*(D164525), doi:10.1029/2003JD003597.

Ciais, P., et al. (1997a), A three-dimensional synthesis study of δ^{18}O in atmospheric CO_2, Part I: Surface fluxes, *J. Geophys. Res.*, *102*, 5857–5872.

Ciais, P., et al. (1997b), A three-dimensional synthesis study of δ^{18}O in atmospheric CO_2, Part II: Simulations with the TM2 transport model, *J. Geophys. Res.*, *102*, 5873–5883.

Collatz, G. J., J. T. Ball, C. Grivet, and J. A. Berry (1991), Physiological and environmental regulation of stomatal conductance, photosynthesis, and transpiration: A model that includes a laminar boundary layer, *Agric. For. Meteorol.*, *54*, 107–136.

Collins, W. D., et al. (2006), The Community Climate System Model: CCSM3, *J. Clim.*, *19*, 2122–2143.

Cooley, H. S., W. J. Riley, M. S. Torn, and Y. He (2005), Impact of agricultural practice on regional climate in a coupled land surface mesoscale model, *J. Geophys. Res.*, *110*, D03113, doi:10.1029/2004JD005160.

Craig, H., and A. Gordon, Deuterium and oxygen 18 variations in the ocean and the marine atmosphere (1965), paper presented at Stable Isotopes in Oceanographic Studies and Paleotemperatures, Cons. Naz. delle Ric. Lab. di Geol. Nucl., Spoleto, Italy.

Cressman, G. P. (1959), An operative objective analysis system, *Mon. Weather Rev.*, *87*, 367–374.

Cuntz, M., P. Ciais, and G. Hoffmann (2002), Modeling the continental effect of oxygen isotopes over Eurasia, *Tellus, Ser. B*, *54*, 895–911, doi:10.1034/j.1600-0899.2002.01341.

Cuntz, M., P. Ciais, G. Hoffman, and W. Knorr (2003a), A comprehensive global three-dimensional model of δ^{18}O in atmospheric CO_2: Part I: Validation of surface processes, *J. Geophys. Res.*, *108*(D174527), doi:10.1029/2002JD003153.

Cuntz, M., P. Ciais, G. Hoffman, C. E. Allison, R. J. Francey, W. Knorr, P. P. Tans, J. W. White, and I. Levin (2003b), A comprehensive global three-dimensional model of δ^{18}O in atmospheric CO_2: Part II: Mapping the atmospheric signal, *J. Geophys. Res.*, *108*(D174528), doi:10.1029/2002JD003154.

Denman, K. L., et al. (2007), Couplings between changes in the climate system and biogeochemistry, in *Climate Change 2007: The Physical Science Basis. Contribution of Working Group I to the Fourth Assessment Report of the Intergovernmental Panel on Climate Change*, edited by S. Solomon et al., pp. 499–587, Cambridge Univ. Press, Cambridge, United Kingdom and New York, NY, USA.

Denning, A. S., G. J. Collatz, C. G. Zhang, D. A. Randall, J. A. Berry, P. J. Sellers, G. D. Colello, and D. A. Dazlich (1996), Simulations of terrestrial carbon metabolism and atmospheric CO_2 in a general circulation model: 1. Surface carbon fluxes, *Tellus, Ser. B*, *48*(4), 521–542.

Dongmann, G., H. W. Nürnberg, H. Förstel, and K. Wagener (1974), On the enrichment of $H_2{}^{18}O$ in the leaves of transpiring plants, *Radiat. Environ. Biophys.*, *11*, 41–52.

Farquhar, G. D., and J. Lloyd (1993), Carbon and oxygen isotope effects in exchange of carbon dioxide between terrestrial plants and the atmosphere, in *Stable Isotopes and Plant Carbon-Water Relations*, edited by J. R. Ehlleringer, A. E. Hall, and G. D. Farquhar, pp. 47–70, Academic, New York.

Farquhar, G. D., J. Lloyd, J. A. Taylor, L. B. Flanagan, J. P. Syvertsen, K. T. Hubick, S. Wong, and J. R. Ehleringer (1993), Vegetation effects on the isotope composition of oxygen in atmospheric CO_2, *Nature*, *363*, 439–443.

Flanagan, L. B. (2005), Ecosystem CO_2 exchange and variation in the δ^{18}O of atmospheric CO_2, in *Stable Isotopes and Biosphere-Atmosphere Interactions, Physiological Ecology*, edited by L. B. Flanagan, J. R. Ehleringer, and D. E. Pataki, pp. 171–181, Elsevier, San Diego, CA.

Flanagan, L. B., J. P. Comstock, and J. R. Ehleringer (1991), Comparison of modeled and observed environmental influences on stable oxygen and hydrogen isotope composition of leaf water in Phaseolus-vulgaris L, *Plant Physiol.*, *96*, 439–443.

Francey, R. J., and P. P. Tans (1987), Latitudinal variation in O-18 of atmospheric CO_2, *Nature*, *327*, 495–497.

Fung, I., et al. (1997), Carbon-13 exchanges between the atmosphere and biosphere, *Global Biogeochem. Cycles*, *11*, 507–533.

Gillon, J. S., and D. Yakir (2000), Naturally low carbonic anhydrase activity in C-4 and C-3 plants limit discriminations against (COO)-O-18 during photosynthesis, *Plant Cell Environ.*, *23*, 903–915.

Gillon, J. S., and D. Yakir (2001), Influence of carbonic anhydrase activity in terrestrial vegetation on the O-18 content of atmospheric CO_2, *Science*, *291*, 2584–2587.

Gu, L., D. D. Baldocchi, S. C. Wofsy, J. W. Munger, J. J. Michalsky, S. P. Urbanski, and T. A. Boden (2003), Response of a deciduous forest to the Mount Pinatubo eruption: Enhanced photosynthesis, *Science*, *299*, 2035–2038.

Gurney, K. R., et al. (2002), Towards robust regional estimates of CO_2 sources and sinks using atmospheric transport models, *Nature*, *415*, 626–630.

Gurney, K. R., et al. (2003), Transcom 3 CO_2 inversion intercomparison: 1. Annual mean control results and sensitivity to transport and prior flux information, *Tellus Ser. B*, *55*, 555–579.

Gurney, K., et al. (2004), Transcom 3 inversion intercomparison: Model mean results for the estimation of seasonal carbon sources and sinks, *Global Biogeochem. Cycles*, *18*, GB1010, doi:10.1029/2003GB002111.

Henderson-Sellers, A., M. Fischer, I. Aleinov, K. McGuffie, W. J. Riley, G. A. Schmidt, K. Sturm, K. Yoshimura, and P. Irannejad (2006), Stable water isotope simulation by current land-surface schemes: Results of iPILPS Phase 1, *Global Planet. Change*, *51*, 34–58, doi:10.1016/J. Gloplacha.2006.01.003.

Hesterberg, R., and U. Siegenthaler (1991), Production and stable isotopic composition of CO_2 in a soil near Bern, Switzerland, *Tellus, Ser. B*, *43*(2), 197–205.

Hoffmann, G., M. Werner, and M. Heimann (1998), The water isotope module of the ECHAM atmospheric general circulation model – A study on time scales from days to several years, *J. Geophys. Res.*, *103*, 16,871–16,896.

Ishizawa, M., T. Nakazawa, and K. Higuchi (2002), A multi-box model study of the role of the biospheric metabolism in the recent decline of δ^{18}O in atmospheric CO_2, *Tellus, Ser. B*, *54*, 307–324.

Isotope Hydrology Section (2006), Global network of isotopes in precipitation. The GNIP Database, http://isohis.iaea.org, Int. At. Energy Agency, Vienna.

Jarvis, P. G. (1976), The interpretation of the variations in leaf water potential and stomatal conductance found in canopies in the field, *Phil. Trans. R. Soc. Lond., Ser. B*, *273*, 593–610.

Johnsen, S. J., W. Dansgaard, and J. W. C. White (1989), The origin of Arctic precipitation under present and glacial conditions, *Tellus, Ser. B*, *41*(4), 452–468, doi:10.1111/j.1600-0889.1989.tb00321.

Jones, H. G., and K. H. Higgs (1989), Empirical models of the conductance of leaves in apple orchards, *Plant Cell Environ.*, *12*, 301–308.

Jouzel, J., G. L. Russel, R. J. Suozzo, R. D. Koster, J. W. C. White, and W. S. Broecker (1987), Simulations of the HDO and $H_2{}^{18}O$ atmospheric cycles using the NASA GISS general circulation model: The seasonal cycle for present-day conditions, *J. Geophys. Res.*, *92*, 14,739–14,760.

Kalnay, E., et al. (1996), The NCEP/NCAR 40-year reanalysis project, *Bull. Am. Meteorol. Soc.*, *77*, 437–470.

Lai, C. T., W. Riley, C. Owensby, J. Ham, A. Schauer, and J. R. Ehleringer (2006), Seasonal and interannual variations of carbon and oxygen isotopes of respired CO_2 in a tallgrass prairie: Measurements and modeling results from 3 years with contrasting water availability, *J. Geophys. Res.*, *111* D08S06, doi:10.1029/2005JD006436.

Lee, X., T. J. Griffis, J. M. Baker, K. A. Billmark, K. Kim, and L. R. Welp (2009), Canopy-scale kinetic fractionation of atmospheric carbon dioxide and water vapor isotopes, *Global Biogeochem. Cycles*, *23*, GB1002, doi:10.1029/2008GB003331.

LeGrande, A. N., and G. A. Schmidt (2006), Global gridded data set of the oxygen isotopic composition in seawater, *Geophys. Res. Lett.*, *33*, L12604, doi:10.1029/2006GL026011.

Luz, B., E. Barkan, R. Yam, and A. Shemesh (2009), Fractionation of oxygen and hydrogen isotopes in evaporating water, *Geochim. Cosmochim. Acta*, *73*, 6697–6703, doi:10.1016/j.gca.2009.08.008.

Majoube, M. (1971), Factionnement en oxygene-18 te en deuterium entre l'eau et sa vapeur, *J. Clim. Phys.*, *58*, 1423–1436.

Mathieu, R., and T. Bariac (1996), A numerical model of the simulation of stable isotope profiles in drying soils, *J. Geophys. Res.*, *101*, 12,685–12,696.

McDowell, N., et al. (2008), Understanding the stable isotope composition of biosphere atmosphere CO$_2$ exchange, *EOS Trans. Am. Geophys. Union*, *89*, 94–95.

Miller, J. B., D. Yakir, J. W. C. White, and P. P. Tans (1999), Measurements of O-18/O-16 in the soil-atmosphere CO$_2$ flux, *Global Biogeochem. Cycles*, *13*, 761–774.

Naegler, T., P. Ciais, K. Rodgers, and I. Levin (2006), Excess radiocarbon constraints on air-sea gas exchange and the uptake of CO$_2$ by the oceans, *Geophys. Res. Lett.*, *33*, L11802, doi:10.1029/2005GL025408.

Nemani, R. R., C. D. Keeling, H. Hashimoto, W. M. Jolly, S. C. Piper, C. J. Tucker, R. B. Myneni, and S. W. Running (2003), Climate-driven increases in global terrestrial net primary production from 1982 to 1999, *Science*, *300*, 1560–1563.

Noone, D., and I. Simmonds (2002), Associations between delta O-18 of water and climate parameters in a simulation of atmospheric circulation for 1979–95, *J. Clim.*, *15*(22), 3150–3169.

Noone, D., and C. Sturm (2010), Comprehensive dynamical models of global and regional water isotope distributions, in *Isoscapes: Understanding Movement, Patterns, and Process on Earth Through Isotope Mapping*, edited by J. West et al., pp. 195–219, Springer, Dordrecht, Netherlands.

Ogée, P. Peylin, M. Cuntz, T. Bariac, Y. Brunet, P. Berbigier, P. R., and P. Ciais (2004), Partitioning net ecosystem carbon exchange into net assimilation and respiration with canopy-scale isotopic measurements: An error propagation analysis with ^{13}CO$_2$ and CO^{18}O, *Global Biogeochem. Cycles*, *18*, GB2019, doi:10.1029/2003GB002166.

Peylin, P., P. Ciais, S. Denning, P. P. Tans, J. A. Berry, and J. W. C. White (1999), A 3-dimensional study of δ^{18}O in atmospheric CO$_2$: Contribution of different land ecosystems, *Tellus, Ser. B*, *51*, 642–667.

Potter, C. S. (1999), Terrestrial biomass and the effects of deforestation on the global carbon cycle, *BioScience*, *49*, 769–778, doi:10.2307/1313568.

Potter, C. S., S. Klooster, and V. Brooks (1999), Interannual variability in terrestrial net primary production: Exploration of trends and controls on regional to global scales, *Ecosyst. (N. Y.)*, *2*, 36–48, doi:10.1007/s100219900056.

Qian, T., A. Dai, K. E. Trenberth, and K. W. Oleson (2006), Simulation of global land surface conditions from 1948–2004. Part I: Forcing data and evaluation, *J. Hydrometeorol.*, *7*, 953–975.

Quay, P. D., B. Tilbrook, and C. S. Wong (1992), Oceanic uptake of fossil fuel CO$_2$: Carbon-13 evidence, *Science*, *256*, 74–79.

Ramonet, M., and P. Monfray (1996), CO$_2$ baseline concept in 3-D atmospheric transport models, *Tellus, Ser. B*, *48*, 502–520.

Rayner, P. J., R. M. Law, C. E. Allison, R. J. Francey, C. M. Trudinger, and C. Pickett-Heaps (2008), Interannual variability of the global carbon cycle (1992–2005) inferred by inversion of atmospheric CO$_2$ and delta(CO$_2$)-C-13 measurements, *Global Biogeochem. Cycles*, *22*, GB3008, doi:10.1029/2007GB003068.

Riley, W. J. (2005), A modeling study of the impact of the delta O-18 value of near-surface soil water on the delta O-18 value of the soil-surface CO$_2$ flux, *Geochem. Cosmochem. Acta*, *69*(8), 1939–1946.

Riley, W. J., C. J. Still, M. Torn, and J. A. Berry (2002), A mechanistic model of H$_2$^{18}O and CO^{18}O fluxes between ecosystems and atmosphere: Model description and sensitivity analyses, *Global Biogeochem. Cycles*, *16*(41095), doi:10.1029/2002GB001878.

Riley, W. J., C. J. Still, B. R. Helliker, M. Ribas-Carbo, and J. A. Berry (2003), ^{18}O composition of CO$_2$ and H$_2$O ecosystem pools and fluxes in a tallgrass prairie: Simulations and comparisons to measurements, *Global Change Biol.*, *9*(11), 1567–1581.

Riley, W. J., J. T. Randerson, P. N. Foster, and T. J. Lueker (2005), Influence of terrestrial ecosystems and topography on coastal CO$_2$ measurements: A case study at Trinidad Head, California, *J. Geophys. Res.*, *110*, G01005, doi:10.1029/2004JG000007.

Robock, A. (2000), Volcanic eruptions and climate, *Rev. Geophys.*, *38*(2), 191–219.

Sarmiento, J. L., and N. Gruber (2002), Sinks for anthropogenic carbon, *Phys. Today*, *55*(8), 30–36.

Smith, T. M., R. W. Reynolds, T. C. Peterson, and J. Lawrimore (2008), Improvements to NOAA's historical merged land–ocean surface temperature analysis (1880–2006), *J. Clim.*, *21*, 2283–2296, doi:10.1175/2007JCLI2100.1.

Stern, L. A., R. Amundson, and W. T. Baisden (2001), Influence of soils on oxygen isotope ratio of atmospheric CO$_2$, *Global Biogeochem. Cycles*, *15*, 753–759.

Stewart, J. B. (1988), Modelling surface conductance of Pine forest, *Agric. For. Meteorol.*, *43*, 19–35.

Still, C. J., et al. (2005), Simulation of ecosystem C18OO isotope fluxes in a tallgrass prairie: Biological and physical controls, in *Stable Isotopes and Biosphere-Atmosphere Interactions*, edited by L. B. Flanagan, J. R. Ehleringer, and D. E. Pataki, pp. 154–170, Elsevier, San Diego, Calif.

Still, C. J., et al. (2009), The influence of clouds and diffuse radiation on ecosystem-atmosphere CO$_2$ and CO^{18}O exchanges, *J. Geophys. Res.*, *114*, G01018, doi:10.1029/2008JG000675.

Suyker, A. E., and S. B. Verma (2001), Year-round observations of the net ecosystem exchange of carbon dioxide in a native tallgrass prairie, *Global Change Biol.*, *7*, 279–289, doi:10.1046/j.1365-2486.2001.00407.x.

Takahashi, T., et al. (2002), Global sea-air CO$_2$ flux based on climatological surface ocean pCO$_2$, and seasonal biological and temperature effects, *Deep Sea Res., Part II*, *49*, 1601–1622.

Tans, P. P. (1998), Oxygen isotopic equilibrium between carbon dioxide and water in soils, *Tellus, Ser. B*, *50*, 163–178.

Van der Werf, G. R., J. T. Randerson, L. Giglio, G. J. Collatz, and P. S. Kasibhatla (2006), Interannual variability in global biomass burning emission from 1997 to 2004, *Atmos. Chem. Phys.*, *6*, 3423–3441.

Vogel, J. C., P. M. Grootes, and W. G. Mook (1970), Isotopic fractionation between gaseous and dissolved carbon dioxide, *Z. Phys.*, *230*, 225–238.

Welp, L. R., R. F. Keeling, H. A. J. Meijer, A. F. Bollenbacher, S. C. Piper, K. Yoshimura, R. J. Francey, C. E. Allison, and M. Wahlen (2011), Interannual variability in the oxygen isotopes of atmospheric CO2 driven by El Nino, *Nature*, *477*, 579–582, doi:10.1038/nature10421.

White, J. and B. Vaughn (2009), University of Colorado, Institute of Arctic and Alpine Research (INSTAAR), stable isotopic composition of atmospheric carbon dioxide (^{13}C and ^{18}O) from the NOAA ESRL Carbon Cycle Cooperative Global Air Sampling Network, 1990–2007, Version: 2009-06-01, Path: ftp://ftp.cmdl.noaa.gov/ccg/co2o18/flask/event/.

Wingate, L., et al. (2009), The impact of soil microorganisms on the global budget of δ^{18}O in atmospheric CO$_2$, *Proc. Natl. Acad. Sci. U. S. A.*, *106*(52), 22,411–22,415, doi:10.1073/pnas.0905210106.

Wong, S. C., I. R. Cowan, and G. D. Farquhar (1978), Leaf conductance in relation to assimilation in *Eucalyptus pauciflora* Sieb. cx Spreng: Influence of irradiance and partial pressure of carbon dioxide, *Plant Physiol.*, *62*, 670–674.

Yoshimura, K., M. Kanamitsu, D. Noone, and T. Oki (2008), Historical isotope simulation using Reanalysis atmospheric data, *J. Geophys. Res.*, *113*(D19), D19108, doi:10.1029/2008JD010074.